The Astrophysical Journal, 741:111 (18pp), 2011 November 10 doi:10.1088/0004-637X/741/2/111

FIRST SEASON QUIET OBSERVATIONS: MEASUREMENTS OF COSMIC MICROWAVE BACKGROUND POLARIZATION POWER SPECTRA AT 43 GHz IN THE MULTIPOLE RANGE $25 \leqslant \ell \leqslant 475$

QUIET Collaboration, C. Bischoff[1,22], A. Brizius[1,2], I. Buder[1], Y. Chinone[3,4], K. Cleary[5], R. N. Dumoulin[6], A. Kusaka[1], R. Monsalve[7], S. K. Næss[8], L. B. Newburgh[6,23], R. Reeves[5], K. M. Smith[1,23], I. K. Wehus[9], J. A. Zuntz[10,11,12], J. T. L. Zwart[6], L. Bronfman[13], R. Bustos[7,13,14], S. E. Church[15], C. Dickinson[16], H. K. Eriksen[8,17], P. G. Ferreira[10], T. Gaier[18], J. O. Gundersen[7], M. Hasegawa[3], M. Hazumi[3], K. M. Huffenberger[7], M. E. Jones[10], P. Kangaslahti[18], D. J. Kapner[1,24], C. R. Lawrence[18], M. Limon[6], J. May[13], J. J. McMahon[19], A. D. Miller[6], H. Nguyen[20], G. W. Nixon[21], T. J. Pearson[5], L. Piccirillo[16], S. J. E. Radford[5], A. C. S. Readhead[5], J. L. Richards[5], D. Samtleben[2,25], M. Seiffert[18], M. C. Shepherd[5], S. T. Staggs[21], O. Tajima[1,3], K. L. Thompson[15], K. Vanderlinde[1,26], R. Williamson[6,27], and B. Winstein[1]

[1] Kavli Institute for Cosmological Physics, Department of Physics, Enrico Fermi Institute, The University of Chicago, Chicago, IL 60637, USA; akito@kicp.uchicago.edu
[2] Max-Planck-Institut für Radioastronomie, 53121 Bonn, Germany
[3] High Energy Accelerator Research Organization (KEK), Tsukuba, Ibaraki 305-0801, Japan
[4] Astronomical Institute, Graduate School of Science, Tohoku University, Aramaki, Aoba, Sendai 980-8578, Japan
[5] Cahill Center for Astronomy and Astrophysics, California Institute of Technology, Pasadena, CA 91125, USA
[6] Department of Physics and Columbia Astrophysics Laboratory, Columbia University, New York, NY 10027, USA
[7] Department of Physics, University of Miami, Coral Gables, FL 33146, USA
[8] Institute of Theoretical Astrophysics, University of Oslo, N-0315 Oslo, Norway
[9] Department of Physics, University of Oslo, N-0316 Oslo, Norway
[10] Department of Astrophysics, University of Oxford, Oxford OX1 3RH, UK
[11] Oxford Martin School, Oxford OX1 3BD, UK
[12] Department of Physics and Astronomy, University College London, London WC1E, UK
[13] Departamento de Astronomía, Universidad de Chile, Casilla 36-D, Santiago, Chile
[14] Departamento de Astronomía, Universidad de Concepción, Casilla 160-C, Concepción, Chile
[15] Kavli Institute for Particle Astrophysics and Cosmology and Department of Physics, Stanford University, Varian Physics Building, Stanford, CA 94305, USA
[16] Jodrell Bank Centre for Astrophysics, Alan Turing Building, School of Physics and Astronomy, The University of Manchester, Manchester M13 9PL, UK
[17] Centre of Mathematics for Applications, University of Oslo, N-0316 Oslo, Norway
[18] Jet Propulsion Laboratory, California Institute of Technology, Pasadena, CA 91109, USA
[19] Department of Physics, University of Michigan, Ann Arbor, MI 48109, USA
[20] Fermi National Accelerator Laboratory, Batavia, IL 60510, USA
[21] Joseph Henry Laboratories of Physics, Jadwin Hall, Princeton University, Princeton, NJ 08544, USA
Received 2010 December 14; accepted 2011 July 12; published 2011 October 25

ABSTRACT

The Q/U Imaging ExperimenT (QUIET) employs coherent receivers at 43 GHz and 94 GHz, operating on the Chajnantor plateau in the Atacama Desert in Chile, to measure the anisotropy in the polarization of the cosmic microwave background (CMB). QUIET primarily targets the B modes from primordial gravitational waves. The combination of these frequencies gives sensitivity to foreground contributions from diffuse Galactic synchrotron radiation. Between 2008 October and 2010 December, over 10,000 hr of data were collected, first with the 19 element 43 GHz array (3458 hr) and then with the 90 element 94 GHz array. Each array observes the same four fields, selected for low foregrounds, together covering ≈1000 deg^2. This paper reports initial results from the 43 GHz receiver, which has an array sensitivity to CMB fluctuations of 69 μK$\sqrt{\text{s}}$. The data were extensively studied with a large suite of null tests before the power spectra, determined with two independent pipelines, were examined. Analysis choices, including data selection, were modified until the null tests passed. Cross-correlating maps with different telescope pointings is used to eliminate a bias. This paper reports the EE, BB, and EB power spectra in the multipole range $\ell = 25$–475. With the exception of the lowest multipole bin for one of the fields, where a polarized foreground, consistent with Galactic synchrotron radiation, is detected with 3σ significance, the E-mode spectrum is consistent with the ΛCDM model, confirming the only previous detection of the first acoustic peak. The B-mode spectrum is consistent with zero, leading to a measurement of the tensor-to-scalar ratio of $r = 0.35^{+1.06}_{-0.87}$. The combination of a new time-stream "double-demodulation" technique, side-fed Dragonian optics, natural sky rotation, and frequent boresight rotation leads to the lowest level of systematic contamination in the B-mode power so far reported, below the level of $r = 0.1$.

Key words: cosmic background radiation – cosmology: observations – gravitational waves – inflation – polarization

Online-only material: color figures, extended figure

[22] Current address: Harvard-Smithsonian Center for Astrophysics, 60 Garden Street MS 43, Cambridge, MA 02138, USA.
[23] Current address: Joseph Henry Laboratories of Physics, Jadwin Hall, Princeton University, Princeton, NJ 08544, USA.
[24] Current address: Micro Encoder Inc., Kirkland, WA 98034, USA.
[25] Current address: Nikhef, Science Park, Amsterdam, The Netherlands.
[26] Current address: Department of Physics, McGill University, 3600 Rue University, Montreal, Quebec H3A 2T8, Canada.
[27] Current address: Kavli Institute for Cosmological Physics, Enrico Fermi Institute, The University of Chicago, Chicago, IL 60637, USA.

1. INTRODUCTION

The inflationary paradigm resolves several outstanding issues in cosmology, including the flatness, horizon, and monopole problems, and it provides a compelling explanation for the origin of structure in the universe (e.g., Liddle & Lyth 2000 and references therein). So far all cosmological data, including measurements of cosmic microwave background (CMB) anisotropies, support this paradigm; still, the underlying fundamental physics responsible for inflation is unknown. Inflation produces a stochastic background of gravity waves that induce odd-parity tensor "B modes" at large angular scales in the CMB polarization. If these primordial B modes, parameterized by the tensor-to-scalar ratio r, are detected, one can learn about the energy scale of inflation. In many attractive slow-roll models, this scale is given approximately by $r^{1/4} \times 10^{16}$ GeV. For large-field models, the energy scale is near the Grand Unification Scale in particle physics, so that $r \gtrsim 0.01$. A new generation of experiments aims for good sensitivity in this range of r. Establishing the existence of primordial B modes would both verify an important prediction of inflation and provide access to physics at an incredibly high energy scale.

The most stringent limit to date is $r < 0.20$ at the 95% confidence level (Komatsu et al. 2011) set by a combination of CMB-temperature-anisotropy measurements, baryon acoustic oscillations, and supernova observations, but cosmic variance prohibits improvements using only these measurements.

E-mode polarization has now been detected by many experiments (e.g., Kovac et al. 2002; Leitch et al. 2005; Montroy et al. 2006; Sievers et al. 2007; Wu et al. 2007; Bischoff et al. 2008; Larson et al. 2011). These measurements are consistent with predictions from CMB-temperature-anisotropy measurements, and they provide new information on the epoch of reionization. Only BICEP has accurately measured E-mode polarization in the region of the first acoustic peak (Chiang et al. 2010); that paper also reports the best limit on r coming from cosmological B modes: $r < 0.72$ at the 95% confidence level.

Experiments measuring B-mode polarization in the CMB should yield the best information on r, but this technique is still in its infancy. B modes are expected to be at least an order of magnitude smaller than the E modes so control of systematic errors and foregrounds will be particularly critical. Below ≈90 GHz, the dominant foreground comes from Galactic synchrotron emission, while at higher frequencies, emission from thermal dust dominates. Most planned or operating CMB polarization experiments employ bolometric detectors observing most comfortably at frequencies $\gtrsim$90 GHz, so they cannot estimate synchrotron contamination from their own data.

The Q/U Imaging ExperimenT (QUIET) is one of two CMB polarization experiments to observe at frequencies suitable for addressing synchrotron contamination, making observations at 43 GHz (Q band) and 94 GHz (W band) and with sufficient sensitivity to begin to probe primordial B modes. The other is *Planck* (Tauber et al. 2010).

QUIET uses compact polarization-sensitive modules based upon High Electron Mobility Transistor (HEMT) amplifiers, combined with a new time-stream "double-demodulation" technique, side-fed Dragonian optics (for the first time in a CMB polarization experiment), natural sky rotation, and frequent rotation about the optical axis to achieve a very low level of contamination in the multipole range where a primordial-B-mode signal is expected.

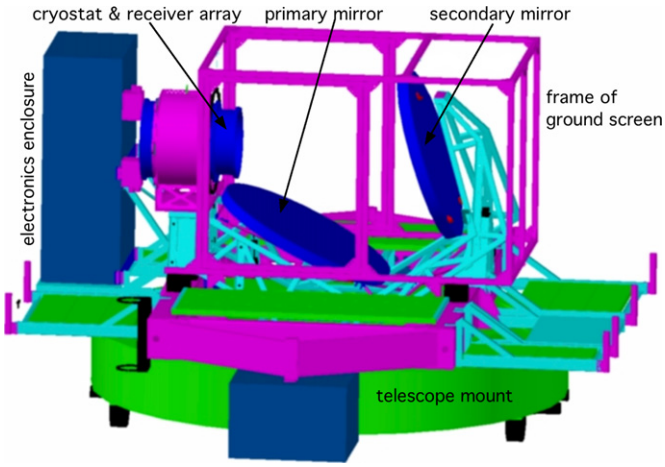

Figure 1. Overview of the QUIET instrument. The cryostat and 1.4 m telescope mirrors are enclosed in a rectangular comoving absorbing ground screen; in this figure its walls are transparent. The telescope, cryostat, and electronics are mounted on a single platform attached to the deck bearing, which allows rotations around the instrument's optical axis.

(A color version of this figure is available in the online journal.)

Between 2008 October and 2010 December, QUIET collected over 10,000 hr of data, split between the Q-band and W-band receivers. Here, we report first results from the first season of 3458 hr of Q-band observation. The principal investigator for QUIET was our recently deceased colleague, Bruce Winstein, whose intellectual and scientific guidance was crucial to QUIET in all of its stages, from design through analysis, through the writing of this paper.

After describing the instrument, observations, and detector calibrations (Sections 2–4), we discuss our analysis techniques and consistency checks (Sections 5 and 6). CMB power spectra are then presented together with a foreground detection (Section 7). We evaluate our systematic errors (Section 8) and then conclude (Section 9).

2. THE INSTRUMENT

The QUIET instrument comprises an array of correlation polarimeters cooled to 20 K and coupled to a dual-reflector telescope, installed on a three-axis mount inside a comoving ground screen. The instrument is illustrated in Figure 1. Further details are given below and in Newburgh (2010), Kusaka (2010), and Buder (2010).

The Q-band QUIET receiver is a 19 element array containing 17 low-noise correlation polarimeters, each simultaneously measuring the Stokes Q, U, and I parameters, and two CMB differential-temperature monitors.

QUIET uses a 1.4 m classical side-fed Dragonian antenna (Dragone 1978). This consists of a parabolic primary, a concave hyperbolic secondary along with a platelet array of corrugated feed horns (Gundersen & Wollack 2009). These elements are oriented in a way to satisfy the Mizuguchi condition (Mizugutch et al. 1976) in order to minimize cross polar response, and unlike dual offset classical Gregorian or Cassegrain antennas, the elements combine to generate high gain with low sidelobe response over a wide field of view (Chang & Prata 2004). The telescope is described in detail in Imbriale et al. (2011). It yields an FWHM beam size of 27′.3 and a roughly circular field of view of 7° in diameter. Radiation from each feed horn enters a septum polarizer (Bornemann & Labay 1995) which separates left and right circularly polarized components (L and R) into

two waveguide ports that mate to a QUIET correlation module, detailed below.

The module array and feed horns are cooled to 20 K in a cryostat to reduce instrumental noise. An electronics enclosure mounted next to the cryostat houses the electronics necessary for biasing the modules and recording their data. The cryostat, electronics, and telescope are installed on the former Cosmic Background Imager mount (Padin et al. 2002). This mount provides three-axis motion: azimuth, elevation, and rotation about the optical axis. This last is called "deck" rotation.

The cryostat and telescope are enclosed by an absorbing comoving ground screen. The ground screen was designed to have two parts, but the upper section (not shown in Figure 1) was not installed until after the Q-band instrument was removed. Its absence was correctly anticipated to result in two far sidelobes, which were mapped with a high-power source by the QUIET W-band instrument in the field and measured to be $\lesssim$–60 dB with the QUIET Q-band instrument when the Sun passed through them. The effects of these sidelobes are mitigated through filtering and data selection (Sections 5.1.3 and 5.2). Section 8.4 shows that any residual contamination is small.

Each QUIET Q-band correlation module, in a footprint of only $5.1 \times 5.1\,\mathrm{cm}^2$, receives the circular polarization modes of the celestial radiation and outputs Stokes Q, U, and I as follows. Each input is independently amplified and passed through a phase switch. One phase switch alternates the sign of the signal voltage at 4 kHz, while the other switches do so at 50 Hz. The two signals are combined in a 180° hybrid coupler, with outputs proportional to the sum and difference of the inputs. Since the module inputs are proportional to $(L, R) = (E_x \pm i E_y)/\sqrt{2}$, where E_x and E_y are orthogonal components of the incident electric field, the coupler outputs are amplified versions of E_x and iE_y, with the phase switch reversing their roles. Half of each output is bandpass filtered and rectified by a pair of detector diodes, while the other half passes into a 90° hybrid coupler. A second pair of bandpass filters and detector diodes measures the power from this coupler's outputs (Kangaslahti et al. 2006).

Synchronous demodulation of the 4 kHz phase switching yields measurements of Stokes $+Q$ and $-Q$ on the first two diodes and Stokes $+U$ and $-U$ on the remaining two. This high-frequency differencing suppresses low-frequency atmospheric fluctuations as well as $1/f$ noise from the amplifiers, detector diodes, bias electronics, and data-acquisition electronics. Subsequent demodulation of the 50 Hz phase switching removes spurious instrumental polarization generated by unequal transmission coefficients in the phase-switch circuits. The resulting four "double-demodulated" time streams are the polarization channels.

Averaging the output of each diode rather than demodulating it results in a measurement of Stokes I, hereafter called total power, denoted "TP." The TP time streams are useful for monitoring the weather and the stability of the detector responsivities, but suffer too much contamination from $1/f$ noise to constrain the CMB temperature anisotropy. Therefore, the Q-band instrument includes two correlation modules that are coupled to a pair of neighboring feed horns to measure the temperature difference between them, in a scheme similar to the *Wilkinson Microwave Anisotropy Probe* (*WMAP*) differencing assemblies (Jarosik et al. 2003). These differential-temperature modules provide calibration data for the telescope pointing, beams, and sidelobes, as well as CMB data. Their feed horns are in the outer ring of the close-packed hexagonal array, ≈3° from the center.

Table 1
Patch Locations and Integration Times

Patch	R.A. (J2000)	Decl. (J2000)	Integration Hours
CMB-1	12^h04^m	$-39°00'$	905
CMB-2	05^h12^m	$-39°00'$	703
CMB-3	00^h48^m	$-48°00'$	837
CMB-4	22^h44^m	$-36°00'$	223
G-1	16^h00^m	$-53°00'$	311
G-2	17^h46^m	$-28°56'$	92

Notes. The central equatorial coordinates and integration times for each observing patch. G-1 and G-2 are Galactic patches.

Here, we summarize several array-wide characteristics of the polarimeters. Bandpass measurements in the lab and at the start of the observing season find that the average center frequency is 43.1 ± 0.4 GHz, and the average bandwidth is 7.6 ± 0.5 GHz. We calculate the noise power spectra of the double-demodulated polarimeter time streams from each 40–90 minute observation to assess their $1/f$ knee frequencies and white-noise levels (see Section 5.1). The median $1/f$ knee frequency is 5.5 mHz, well below the telescope scan frequencies of 45–100 mHz.

From the white-noise levels and responsivities (Section 4.1), we find an array sensitivity[28] to CMB fluctuations of 69 $\mu\mathrm{K}\sqrt{\mathrm{s}}$, such that the mean polarized sensitivity per module is 280 $\mu\mathrm{K}\sqrt{\mathrm{s}}$.

3. OBSERVATIONS

QUIET is located on the Chajnantor plateau in the Atacama Desert of northern Chile (67°45′42″W, 23°01′42″S). A combination of high altitude (5080 m) and extreme dryness results in excellent observing conditions for most of the year. During the eight months of QUIET Q-band observations, the median precipitable water vapor (PWV) measured at the nearby Atacama Pathfinder Experiment site (Güsten et al. 2006) was 1.2 mm.

We began observations with the Q-band receiver on 2008 October 24, and took 3458 hr of data until 2009 June 13 (when the receiver was replaced on the telescope by the 90 element W-band receiver). Of these data, 77% are for CMB, with 12% of the observing time used for Galactic fields, 7% for calibration sources, and 4% cut due to obvious instrumental problems such as lack of telescope motion. We observe 24 hr a day, except when interrupted. Our full-season operating efficiency is 63%; causes of downtime include occasional snow, power outages, and mechanical failures.

3.1. Field Selection

We observe four CMB fields, referred to henceforth as "patches." Table 1 lists their center positions and total integration times, while Figure 2 indicates their positions on the sky.[29] The number of patches is determined by the requirement to always have one patch above the lower elevation limit of the mount (43°). The specific positions of each patch were chosen to minimize foreground emission using *WMAP* three-year data. The area of each patch is $\approx 250\,\mathrm{deg}^2$. In addition to the four

[28] This is the sensitivity for 62 polarization channels. Six of 68 polarization channels are non-functional—an array yield of 92%.

[29] Patch CMB-3 partially overlaps with the field the BICEP collaboration has observed for CMB analysis (Chiang et al. 2010). The data may be used for future analysis cross-correlating maps from the two experiments.

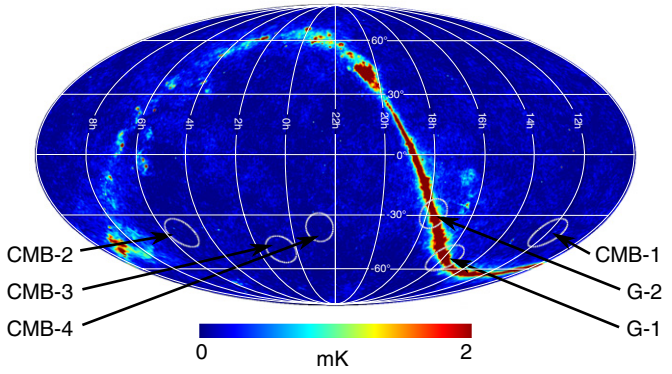

Figure 2. CMB and Galactic patches, in equatorial coordinates, superimposed on a *Q*-band all-sky *WMAP* seven-year temperature map (Jarosik et al. 2010). Note that the Galactic-plane temperature signal saturates the color scale. Patch G-2 is the Galactic center.

(A color version of this figure is available in the online journal.)

CMB patches, we observe two Galactic patches. These allow us to constrain the spectral properties of the polarized low-frequency foregrounds with a high-signal-to-noise ratio. The results from the Galactic observations will be presented in a future publication.

3.2. Observing Strategy

Scanning the telescope modulates the signal from the sky, converting CMB angular scales into frequencies in the polarimeter time streams. Since QUIET targets large angular scales, fast scanning ($\approx 5^\circ$ s^{-1} in azimuth) is critical to ensure that the polarization modes of interest appear at higher frequencies than the atmospheric and instrumental $1/f$ knee frequencies.

So that each module sees a roughly constant atmospheric signal, QUIET scans are periodic motions solely in azimuth with both the elevation and deck-rotation axes fixed. Each scan has an amplitude of $7.^\circ 5$ on the sky, with period 10–22 s. These azimuth scans are repeated for 40–90 minutes; each set of scans at fixed elevation is denoted a "constant-elevation scan" (CES). We repoint the telescope and begin a new CES when the patch center has moved by 15° in order to build up data over an area of $\approx 15^\circ \times 15^\circ$ for each patch. Note that a central region $\simeq 8^\circ$ across is observed by all polarimeters since the instrument's field of view has a diameter of $\simeq 7^\circ$. Diurnal sky rotation and weekly deck rotations provide uniform parallactic-angle coverage of the patch, and ensure that its peripheral regions are also observed by multiple polarimeters.

4. CALIBRATION

Four quantities are required to convert polarimeter time streams into polarization power spectra: detector responsivities, a pointing model, detector polarization angles, and beam profiles. To this end, a suite of calibration observations is performed throughout the season using astronomical sources (Taurus A—hereafter Tau A, Jupiter, Venus, RCW38, and the Moon), atmospheric measurements ("sky dips," which typically consist of three elevation nods of $\pm 3^\circ$), and instrumental sources (a rotating sparse wire grid and a polarized broadband noise source). From these we also measure instrumental polarization, as described below. QUIET's regular calibration observations are summarized in Table 2.

We typically use two or more methods to determine a calibration constant, taking the spread among the methods as an indication of the uncertainty. We show in Section 8 that aside from the case of absolute responsivity, all calibration uncertainties lead to estimates of systematic effects on the power spectra well below statistical errors. This immunity comes from having a large number of detectors and highly cross-linked polarization maps.

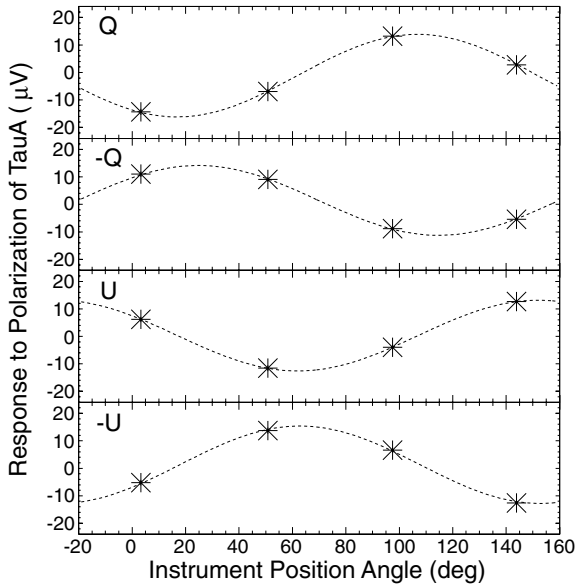

Figure 3. Polarimeter responses from the central feed horn to the polarization of Tau A at four deck angles. The horizontal axis corresponds to the position angle of the receiver focal plane in equatorial coordinates. These data were collected with one correlation module in about 20 minutes. The errors are smaller than the points. From top to bottom, responses are shown for the detector diodes sensitive to the Stokes parameters $+Q$, $-Q$, $+U$, and $-U$, respectively. For each, the fitted model is plotted as a dashed line.

Table 2
Regular Calibration Observations

Source	Schedule	Duration (minutes)
Sky dips	Every 1.5 hr	3
Tau A	Every 1–2 days	20
Moon	Weekly	60
Jupiter	Weekly	20
Venus	Weekly	20
RCW38	Weekly	20

4.1. Responsivity

The polarized flux from Tau A provides a 5 mK signal which we observe at four parallactic angles. The sinusoidal modulation of the signal induced by the changing parallactic angles is fitted to yield responsivity coefficients for each detector. Figure 3 shows the response of the four polarization channels from the central feed horn to Tau A. A typical responsivity is 2.3 mV K^{-1}, with a precision from a single set of observations of 6%. The absolute responsivity from Tau A was measured most frequently for the central feed horn. We choose its $+Q$ diode detector to provide the fiducial absolute responsivity.

The responsivities of other detectors relative to the fiducial detector are determined with the sky dips as described below. We have three independent means of assessing the relative responsivities among polarimeters: from nearly simultaneous measurements of the Moon, from simultaneous measurements of responses to the rotating sparse wire grid in post-season tests,

and from Tau A measurements. The errors from these methods are 4%, 2%, and 6%, respectively, while the error from the sky-dip method is 4%. All the methods agree within errors.

Sky dips generate temperature signals of several 100 mK and thus permit measurement of the TP responsivities. The signals vary slightly with PWV. We estimate the slope from the data as 4% mm^{-1} and correct for it. This slope is consistent with the atmospheric model of Pardo et al. (2001). Because the ratios of the responsivities for the TP and polarized signals from each detector diode are stable quantities within a few percent of unity, we use sky dips performed immediately before each CES to correct short-term variations in the polarimeter responsivities. The responsivities vary by $\lesssim$10% over the course of a day due to changing thermal conditions for the bias electronics. Further post-season tests provide a physical model: the relevant temperatures are varied intentionally while the responsivities are measured with sky dips. We confirm the results with the polarized broadband source.

We bound the uncertainty in the absolute responsivity of the polarimeter array at 6%. The largest contributions to this estimate are uncertainties in (1) the beam solid angle (4%, see below), (2) the response difference between polarized and TP signals for each diode detector (3%), and (3) the Tau A flux (3%; Weiland et al. 2011). The first enters in converting the flux of Tau A into μK, while the second enters because, although one fiducial diode detector is calibrated directly from Tau A, for the rest we find relative responsivities from sky dips and normalize by the fiducial diode's responsivity.

For the differential-temperature modules, all detectors observe the signal from Jupiter simultaneously, providing the absolute responsivity for all channels upon comparison with the Jupiter flux from Weiland et al. (2011). Observations of Venus (Hafez et al. 2008) and RCW38 agree with the Jupiter measurements within errors, and sky dips track short-term variations. We calibrate the absolute responsivity with 5% accuracy.

4.2. Pointing

The global pointing solution derives from a physical model of the three-axis mount and telescope tied to observations of the Moon with the central feed horn in the array, as well as Jupiter and Venus with the differential-temperature feed horns. Optical observations are taken regularly with a co-aligned star camera and used to monitor the time evolution of the pointing model.

During the first two months in the season, a mechanical problem with the deck-angle encoder resulted in pointing shifts. The problem was subsequently repaired. Based on pointing observations of the Moon and other astronomical sources, we verify that these encoder shifts are less than 2°. Systematic uncertainties induced by this problem are discussed in Section 8.1.

After the deck-angle problem is fixed, no significant evolution of the pointing model is found. The difference in the mean pointing solution between the start and the end of the season is smaller than 1′. Observations of the Moon and Jupiter also provide the relative pointing among the feed horns. The rms pointing error in the maps is 3.′5.

4.3. Detector Polarization Angles

Our primary measurement of the polarization angle for each detector comes from observing the radial polarization of the Moon, as illustrated in Figure 4. The measurement has a high signal-to-noise ratio and its inaccuracy is dominated by systematic error due to the temperature gradient of the Moon surface. One can see the effect in the different amplitudes of the two positive envelopes in Figure 4. The fluctuations of the detector polarization-angle measurements over many observations with different phases of the Moon and telescope orientations are typically 1° in rms. Although simulations suggest these fluctuations can be due to the failure to account in analysis for the temperature gradient, we conservatively assign them as upper limits on the fluctuations of the polarization angles during the season. Based on this conservative limit, we estimate the systematic error in the CMB-power-spectra measurement in Section 8.2, resulting in a negligible contribution.

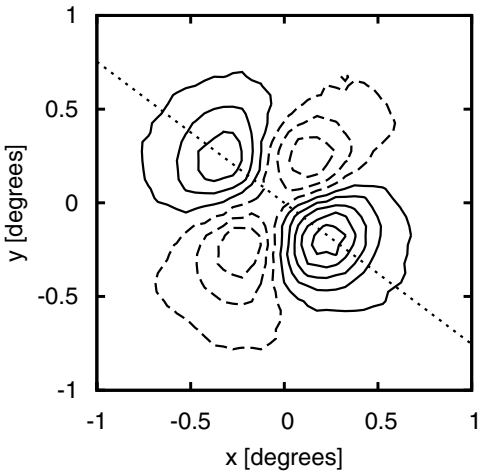

Figure 4. Map of the polarization of the Moon from one detector diode. The amplitude of the quadrupole polarization visible here is ≈400 mK. Similar maps are produced for all 17 polarization modules in the array with a single ≈ hour-long observation. The dotted line indicates the polarization orientation of the detector. Contours are spaced at intervals of 100 mK, with negative contours indicated by dashed lines.

Two other less precise methods also give estimates of the detector angles: fits to the Tau A data, and the determination of the phases of the sinusoidal responses of all the detectors to rotation of the sparse wire grid. In each case, the differences between the detector angles determined by the secondary method and the Moon are described by a standard deviation of ≈3°. However, we find a mean shift between the Tau A derived and Moon-derived angles of 1.°7. To estimate the errors in the angles in light of this shift, we use an empirical approach: in Section 8.2 we estimate the impact on the power spectra from using the Tau A results instead of the Moon results, and find it to be small.

4.4. Beam Profile and Window Function

The polarization and differential-temperature beams are obtained from maps created using the full data sets of Tau A and Jupiter observations, respectively, with square pixels of 1.′8 on a side. For polarization, this process produces the main and leakage beam maps simultaneously, with the latter describing the instrumental polarization. The average FWHM for the beams across the array is 27.′3, measured with 0.′1 precision for the central feed horn and for the differential-temperature feed horns at the edge of the focal plane. The non-central–polarization-horn FWHMs are measured less frequently and thus are less precisely known, with an uncertainty of 1.′5. The beam elongation is typically small (1%), and its effect is further reduced by the diurnal sky rotation and weekly deck rotations which result in a symmetrized effective beam in the CMB maps. We compute one-dimensional symmetrized beam profiles, with a

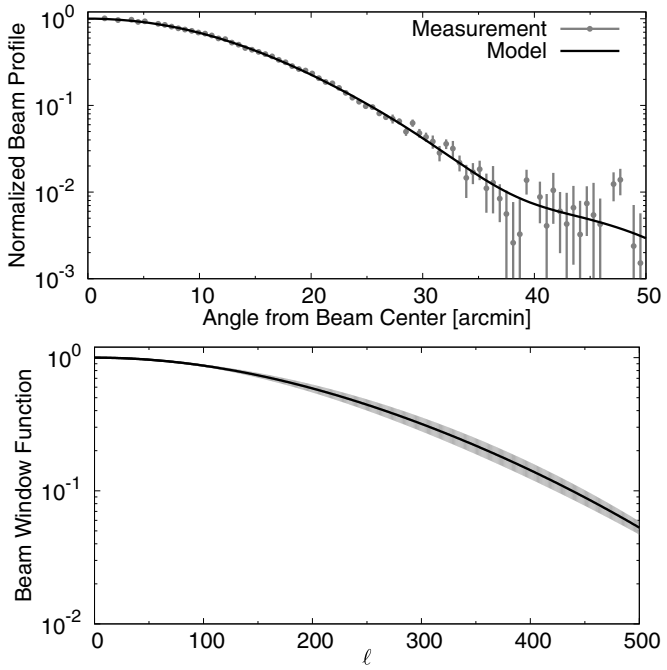

Figure 5. Top panel: polarization beam profile from Tau A observations with the central feed horn. The data are overplotted with the expansion in Gauss–Hermite polynomials described in the text. Bottom panel: beam window function with errors shown by the gray band.

resolution of 0.′6. These profiles are modeled as a sum of six even Gauss–Hermite terms (Monsalve 2010). The main-beam solid angles are computed by integrating these models out to 54′ (roughly −28 dB), yielding $78.0 \pm 0.4\,\mu$sr for the differential-temperature horns and $74.3 \pm 0.7\,\mu$sr for the central horn. An average gives $76\,\mu$sr for all horns in the array. We also examine alternative estimates such as integrating the raw beam map instead of the analytical fit. We assign a systematic uncertainty of 4% based on the differences among these different estimates. The systematic error includes possible contributions from sidelobes, which we constrain to $0.7 \pm 0.4\,\mu$sr with antenna range measurements carried out before the observation season.

The window functions, encoding the effect of the finite resolution of the instrument on the power spectra, are computed from the central-horn and the temperature-horn–profile models. The central-horn beam profile and window function are shown in Figure 5. The uncertainty accounts for statistical error and differences between polarization and differential-temperature beams, as described in Section 8.1.

4.5. Instrumental Polarization

Instrumental imperfections can lead to a spurious polarization signal proportional to the unpolarized CMB temperature anisotropy. We call this the I to Q (or U) leakage term. In our instrument, a fraction of the power input on one port of the correlation module is reflected because of a bandpass mismatch to the septum polarizer, and a fraction of the reflected power reenters the other port. The dominant monopole term comes from this effect. We measure the monopole term from the polarimeter responses to temperature changes, using sky dips; Moon, Tau A, and Galactic signals; as well as variations from the weather. The average magnitude is 1.0% (0.2%) for the Q (U) diodes. Note that the discrepancy in the Q and U averages was predicted from measurements of the properties of the septum polarizers and confirmed in the field. We do not correct for this effect but assign systematic errors as described in Section 8.3.

5. DATA ANALYSIS PROCEDURE

QUIET employs two independent analysis pipelines to derive CMB power spectra. We present the methods used for analysis in each pipeline, including data selection, filtering, map making, and power-spectra estimation.

Pipeline A is based on the pseudo-C_ℓ analysis framework, first described by Hivon et al. (2002), which is used by numerous experiments (Netterfield et al. 2002; Brown et al. 2009; Chiang et al. 2010; Larson et al. 2011; Lueker et al. 2010). This pipeline made all analysis choices in accordance with a strict (blind) analysis validation policy described in Section 6. An advantage of the pseudo-C_ℓ framework is computational efficiency, which is critical for completing the more than 30 iterations of the null-test suite. For the same reason, this pipeline is used for the systematic-error evaluations found in Section 8. Pseudo-C_ℓ analysis also enables us to perform cross-correlation, making the resultant power spectra immune to possible misestimation of noise bias.

Pipeline B implements a maximum-likelihood framework (e.g., Tegmark 1997; Bond et al. 1998), which has a long history of use by CMB experiments (e.g., Mauskopf et al. 2000; Page et al. 2007; Wu et al. 2007; Bischoff et al. 2008). This framework yields minimum-variance estimates of the power spectra, naturally accounts for E/B mixing, and directly provides the exact CMB likelihood required for estimation of cosmological parameters, without the use of analytical approximations. In addition to power spectra, it produces unbiased maps with full noise-covariance matrices, useful for comparisons with other experiments. On the other hand, this approach is also computationally more expensive than the pseudo-C_ℓ framework, and a reduced set of null tests is therefore used to evaluate data consistency.

The processing of the time-ordered data (TOD) and the methodology used for data selection are treated in Sections 5.1 and 5.2, respectively. Brief descriptions of the pseudo-C_ℓ and maximum-likelihood techniques are found in Section 5.3. TOD processing, data selection, and analysis for temperature-sensitive modules are discussed in Section 5.4.

5.1. Time-ordered-data Processing

To prepare the TOD for map making, we execute three steps: pre-processing, noise modeling, and filtering. Of these steps, only the filtering is significantly different between the two pipelines.

5.1.1. Pre-processing

The first data-processing step is to correct for a small nonlinearity that was discovered in the analog-to-digital converter (ADC) system. The nonlinearities occur every 1024 bits; roughly 14% of the data are affected. Systematic uncertainty from this effect is estimated in Section 8.5. Next, the receiver data are synchronized with the telescope pointing. The double-demodulation step, described in Section 2, is applied, reducing the sample rate from 100 Hz to 50 Hz. A model of the detectors' polarized responsivities converts the data from ADC counts into thermodynamic temperature. The two pipelines use different responsivity models. Pipeline A applies a constant responsivity throughout each CES, addressing possible variability within a CES as part of the systematic error (Section 8); pipeline

B updates responsivities on two-minute timescales (Dumoulin 2010).

5.1.2. Noise Model

After pre-processing, the time streams for each detector diode in each CES are Fourier-transformed and their noise power spectra are fit to a model[30] with three parameters: the amplitude of white noise, the $1/f$ knee frequency, and the power-law slope of the $1/f$ noise. We also compute the white-noise correlations among detector diodes in the same module: the most important are between the two Q or the two U detector diodes (with an average coefficient of 0.22). A small fraction of the noise spectra contain features not accounted for in the noise model: beam sidelobes (see Section 2) scanning across features on the ground create a narrow spike at the scan frequency; slowly changing weather patterns during a CES create a broader peak also at the scan frequency; and there are some narrow spikes at high ($\gtrsim$6 Hz) frequencies. To prevent these features from biasing the noise model, the fit excludes a region around the scan frequency as well as frequencies above 4.6 Hz. In addition to the noise-model parameters, several statistics quantifying the agreement between the data and noise model are also used for data selection as described in Section 5.2.

5.1.3. Filtering

In pipeline A, three filters are applied. These were chosen from the results of many runs of the null-test suite (see Section 6). First, to remove the high-frequency narrow spikes, we apply a low-pass filter that cuts signals off sharply above 4.6 Hz.[31] Second, to suppress contamination from atmospheric fluctuations and detector $1/f$ noise, we subtract a linear function from each telescope half-scan (left-going or right-going) removing modes below twice the scan frequency.[32] The third filter, designed to eliminate signal from ground emission, removes any azimuthal structure that remains after summing over all half-scans in the CES.

In pipeline B, an apodized bandpass filter is used that accepts modes from 2.5 times the scan frequency to 4.5 Hz; the high-pass component of this filter is designed to suppress scan-synchronous contamination. Further, a time-independent ground-emission model is subtracted. The model of ground emission is generated by building low-resolution and high-signal-to-noise maps in horizon coordinates from the full-season data for each deck angle and module, using large (55′) pixels. Only features that are stable in time, azimuth, elevation, and deck angle contribute to this model. The amplitude of the ground correction is $\lesssim$1 μK.

5.2. Data Selection

The fundamental unit of data used for analysis is the double-demodulated output of one detector diode for a single CES, referred to as a "CES-diode." Selecting only those CES-diodes that correspond to good detector performance and observing conditions is a critical aspect of the data analysis. The data-selection criteria began with a nominal set of cuts and evolved into several distinct configurations, as many as 33 in the case of pipeline A. For each configuration, analysis validation (see Section 6) was performed yielding statistics quantifying the lack of contamination in the data set. The final data set was chosen when these statistics showed negligible contamination and were little affected by changes to the cuts.

Table 3
Total Hours Observed and Data-selection Efficiencies

Patch	Total Hours	A (%)	B (%)	Common (%)
CMB-1	905	81.7	84.3	76.7
CMB-2	703	67.3	70.0	61.2
CMB-3	837	56.0	61.4	51.4
CMB-4	223	70.6	74.2	65.9
All patches	2668	69.4	72.9	64.2

Notes. Selection efficiencies for each pipeline. "Common" gives the efficiencies if both sets of cuts were applied.

Cut efficiencies, defined as the fractions of CES-diodes accepted for the analysis, are given for both pipelines in Table 3. While each pipeline applies its own cuts uniformly to all four patches, the efficiencies among patches are non-uniform because of differences in weather quality. Over the course of the eight-month observing season, patch CMB-1 is primarily visible at night, when the atmosphere tends to be more stable; patch CMB-3 is mostly observed during the day.

The first step of the data selection is simply to remove known bad data: data from six non-functional detector diodes, data during periods of mount malfunctions, and CESs lasting less than 1000 s. Furthermore, we cut individual CES-diodes that show deviation from the expected linear relationship between the demodulated and TP signals. This cut removes data with poor thermal regulation of the electronics or cryostat, or residual ADC nonlinearity.

The beam sidelobes, described in Section 2, introduce contamination to the data if the telescope scanning motion causes them to pass over the ground or the Sun. Ground pickup is dealt with by filtering as described in Section 5.1.3. The less frequent cases of Sun contamination are handled by cutting those CES-diodes for which the Sun's position overlaps with the measured sidelobe regions for each diode.

Additional cuts are specific to each pipeline. Pipeline A removes data taken during bad weather using a statistic calculated from fluctuations of the TP data during 10 s periods, averaged across the array. This cut removes entire CESs. Several more cuts remove individual CES-diodes. While these additional cuts are derived from the noise modeling statistics, they also target residual bad weather. During such marginal weather conditions only some channels need to be cut, since the sensitivity for a given detector diode to atmospheric fluctuations depends on its level of instrumental polarization. Next, we reject CES-diodes with poor agreement between the filtered data and the noise model in three frequency ranges: a narrow range (only 40 Fourier modes) about the scan frequency, from twice the scan frequency to 1 Hz, and from 1 Hz to 4.6 Hz. We also cut CES-diodes that have higher than usual $1/f$ knee frequencies, or large variations during the CES in the azimuthal slopes of the double-demodulated time streams; both these cuts help to eliminate bad weather periods. Finally, we also remove any CES-diodes with an outlier greater than 6σ in the time domain on three timescales (20 ms, 100 ms, and 1 s).

For pipeline B, the weather cut rejects CESs based on a statistic computed from fluctuations of the double-demodulated

[30] At the level of a single CES, the TOD of each detector diode are dominated by noise; the contribution of the CMB is negligible.
[31] For QUIET's beam size and scanning speed a low-pass filter of 4.5–4.6 Hz results in a minimal loss of sensitivity to the CMB.
[32] Typical scan frequencies range from 45 mHz to 100 mHz.

signals from the polarization modules on 10 s and 30 s timescales. Three cuts are applied to remove individual CES-diodes. The first is a cut on the $1/f$ knee frequency, similar to that of pipeline A. Second, a cut is made on the noise model χ^2 in the frequency range passed by the filter, and third, we reject CES-diodes having a large χ^2 in the azimuth-binned TOD. This cut rejects data with possible time variation in the ground signal. Finally, an entire CES is removed if more than 40% of its detectors have already been rejected.

5.3. Map Making and Power-spectra Estimation

After filtering, the TOD for all diodes are combined to produce Q and U maps for each of the QUIET patches. The maps use a HEALPix $N_{\rm side} = 256$ pixelization (Gorski et al. 2005; http://healpix.jpl.nasa.gov/). This section describes the map making and power-spectra estimation from the maps for each of the pipelines.

5.3.1. Pipeline-A Map Making

Polarization maps (Q and U) are made by summing samples into each pixel weighted by their inverse variance, calculated from the white-noise amplitudes. The full covariance matrix is not calculated. Two polarized sources, Centaurus A and Pictor A, are visible in the maps and are removed using circular top-hat masks with radii of 2° and 1°, respectively.

Separate maps are made for each range of telescope azimuth and deck-angle orientations. The coordinates are binned such that there are 10 divisions in azimuth[33] and six distinct ranges of deck-angle orientation. Making separate maps for different telescope pointings enables the cross-correlation described in the next section.

5.3.2. Power-spectra Estimation in Pipeline A

The MASTER (Monte Carlo Apodized Spherical Transform Estimator) method is used in pipeline A (Hivon et al. 2002; Hansen & Gorski 2003); it is based on a pseudo-C_ℓ technique and takes account of effects induced by the data processing using Monte Carlo (MC) simulations. The pseudo-C_ℓ method allows estimation of the underlying C_ℓ using spherical-harmonics transformations when the observations do not cover the full sky uniformly (Wandelt et al. 2001). The pseudo-C_ℓ spectrum, designated by $\tilde{C}_\ell$, is related to the true spectrum C_ℓ by

$$\langle \tilde{C}_\ell \rangle = \sum_{\ell'} M_{\ell\ell'} F_{\ell'} B^2_{\ell'} \langle C_{\ell'} \rangle. \quad (1)$$

There is no term corresponding to noise bias, which would arise if we did not employ a cross-correlation technique. Here, B_ℓ is the beam window function, described in Section 4.4, and $M_{\ell\ell'}$ is a mode-mode-coupling kernel describing the effect of observing only a small fraction of the sky with non-uniform coverage. It is calculable from the pixel weights, which are chosen to maximize the signal-to-noise ratio (Feldman et al. 1994). We bin in ℓ and recover C_ℓ in nine band powers, C_b, and F_ℓ is the transfer function (displayed in Section 7) due to filtering of the data; its binned estimate, F_b, is found by processing noiseless CMB simulations through pipeline A and used to obtain C_b. For the polarization power spectra, Equation (1) is generalized for the case where $\tilde{C}_\ell$ contains both $\tilde{C}^{\rm EE}_\ell$ and $\tilde{C}^{\rm BB}_\ell$.

[33] The azimuth divisions are the same for all patches, which means that not all divisions are populated for patches CMB-3 and CMB-4.

In the power-spectra estimates, we include only the cross-correlations among pointing-division maps, excluding the auto-correlations. Because the noise is uncorrelated for different pointing divisions, the cross-correlation technique allows us to eliminate the noise-bias term and thus the possible residual bias due to its misestimate. Cross-correlation between different pointing divisions also suppresses possible effects of ground contamination and/or time-varying effects. Dropping the auto-correlations creates only a small increase in the statistical errors ($\approx$3%) on the power spectra.

The errors estimated for the pipeline-A power spectra are frequentist two-sided 68% confidence intervals. A likelihood function used to compute the confidence intervals is modeled following Hamimeche & Lewis (2008) and calibrated using the MC simulation ensemble of more than 2000 realizations with and without CMB signal. We also use the likelihood function to put constraints on r and calculate the consistency to ΛCDM.

The partial sky coverage of QUIET generates a small amount of E/B mixing (Challinor & Chon 2005), which contributes an additional variance to the BB power spectrum. We incorporate it as part of the statistical error. This mixing can be corrected (Smith & Zaldarriaga 2007) in future experiments where the effect is not negligible compared to instrumental noise.

5.3.3. Pipeline-B Map Making

In pipeline B, the pixel-space sky map $\hat{\mathbf{m}}$ ($N_{\rm side} = 256$) is given by

$$\hat{\mathbf{m}} = (\mathbf{P}^T\mathbf{N}^{-1}\mathbf{F}\mathbf{P})^{-1}\mathbf{P}^T\mathbf{N}^{-1}\mathbf{F}\mathbf{d}, \quad (2)$$

where $\mathbf{P}$ is the pointing matrix, $\mathbf{N}$ is the TOD-noise-covariance matrix, $\mathbf{F}$ corresponds to the apodized bandpass filter discussed in Section 5.1.3, and $\mathbf{d}$ denotes the TOD. This map is unbiased, and for the case $\mathbf{F} = \mathbf{1}$ it is additionally the maximum-likelihood map, maximizing

$$\mathcal{L}(\mathbf{m}|\mathbf{d}) = e^{-\frac{1}{2}(\mathbf{d}-\mathbf{P}\mathbf{m})^T\mathbf{N}^{-1}(\mathbf{d}-\mathbf{P}\mathbf{m})}. \quad (3)$$

The corresponding map–noise-covariance matrix (e.g., Tegmark 1997; Keskitalo et al. 2010) is

$$\mathbf{N}_{\hat{\mathbf{m}}} = (\mathbf{P}^T\mathbf{N}^{-1}\mathbf{F}\mathbf{P})^{-1}(\mathbf{P}^T\mathbf{F}^T\mathbf{N}^{-1}\mathbf{F}\mathbf{P})(\mathbf{P}^T\mathbf{N}^{-1}\mathbf{F}\mathbf{P})^{-1}. \quad (4)$$

Note that one often encounters the simplified expression $\mathbf{N}_{\hat{\mathbf{m}}} = (\mathbf{P}^T\mathbf{N}^{-1}\mathbf{F}\mathbf{P})^{-1}$ in the literature. This corresponds effectively to assuming that $\mathbf{F} = \mathbf{F}^2$ in the Fourier domain, and is strictly valid for top-hat–filter functions only. For our filters, we find that the simplified expression biases the map-domain $\chi^2 (\equiv \hat{\mathbf{n}}^T\mathbf{N}^{-1}_{\hat{\mathbf{m}}}\hat{\mathbf{n}}$, where $\hat{\mathbf{n}}$ is a noise-only map) by $\approx 3\sigma$, and we therefore use the full expression, which does lead to an unbiased χ^2.

Equations (2)–(4) apply to both polarization and temperature analysis. The only significant difference lies in the definition of the pointing matrix, $\mathbf{P}$. For polarization, $\mathbf{P}$ encodes the detector orientation, while for temperature it contains two entries per time sample, +1 and −1, corresponding to the two horns in the differential-temperature assembly.

After map making, the maps are post-processed by removing unwanted pixels (i.e., compact sources and low-signal-to-noise edge pixels). All 54 compact sources in the seven-year *WMAP* point source catalog (Gold et al. 2011) present in our four patches are masked out, for a total of 4% of the observed area. We also marginalize over large-scale and unobserved modes by projecting out all modes with $\ell \leqslant 5$ ($\ell \leqslant 25$ for temperature) from the noise-covariance matrix using the Woodbury formula, assigning infinite variance to these modes.

5.3.4. Power-spectra Estimation in Pipeline B

Given the unbiased map estimate, $\hat{\mathbf{m}}$, and its noise-covariance matrix, $\mathbf{N}_{\hat{\mathbf{m}}}$, we estimate the binned CMB power spectra, C_b, using the Newton–Raphson optimization algorithm described by Bond et al. (1998), generalized to include polarization. In this algorithm, one iterates toward the maximum-likelihood spectra by means of a local quadratic approximation to the full likelihood. The iteration scheme in its simplest form is

$$\delta C_b = \frac{1}{2}\sum_{b'} \mathcal{F}^{-1}_{bb'} \mathrm{Tr}[(\hat{\mathbf{m}}\hat{\mathbf{m}}^T - \mathbf{C})(\mathbf{C}^{-1}\mathbf{C}_{,b'}\mathbf{C}^{-1})], \quad (5)$$

where b denotes a multipole bin, $\mathbf{C}$ is the signal-plus-noise pixel-space covariance matrix, and $\mathbf{C}_{,b}$ is the derivative of $\mathbf{C}$ with respect to C_b. The signal component of $\mathbf{C}$ is computed from the binned power spectra, C_b, and the noise component is based on the noise model described in Section 5.1.2, including diode–diode correlations. Finally,

$$\mathcal{F}_{bb'} = \frac{1}{2}\mathrm{Tr}(\mathbf{C}^{-1}\mathbf{C}_{,b}\mathbf{C}^{-1}\mathbf{C}_{,b'}) \quad (6)$$

is the Fisher matrix. Additionally, we introduce a step length multiplier, α, such that the actual step taken at iteration i is $\alpha\,\delta C_b$, where $0 < \alpha \leqslant 1$ guarantees that $\mathbf{C}$ is positive definite. We adopt the diagonal elements of the Fisher matrix as the uncertainties on the band powers.

We start the Newton–Raphson search at $C_\ell = 0$, and iterate until the change in the likelihood value is lower than 0.01 times the number of free parameters, corresponding roughly to a 0.01σ uncertainty in the position of the multivariate peak. Typically, we find that 3–10 iterations are required for convergence.

Estimation of cosmological parameters, θ, is done by brute-force grid evaluation of the pixel-space likelihood,

$$\mathcal{L}(\theta) \propto \frac{-(1/2)\mathbf{d}^T\mathbf{C}^{-1}(\theta)\mathbf{d}}{\sqrt{|\mathbf{C}(\theta)|}}. \quad (7)$$

Here, $\mathbf{C}(\theta)$ is the covariance matrix evaluated with a smooth spectrum, C_ℓ, parameterized by θ. In this paper, we only consider one-dimensional likelihoods with a parameterized spectrum of the form $C_\ell = a\,C_\ell^{\mathrm{fid}}$, a being a scale factor and C_ℓ^{fid} a reference spectrum; the computational expense is therefore not a limiting factor. Two different cases are considered, with a being either the tensor-to-scalar ratio, r, or the amplitude of the EE spectrum, q, relative to the ΛCDM model.

5.4. Temperature Data Selection and Analysis

As described in Section 2, we dedicate one pair of modules to differential-temperature measurements. While these modules are useful for calibration purposes, when combined with our polarization data they also enable us to make self-contained measurements of the TE and TB power spectra.

For temperature, both pipelines adopt the pipeline-A data-selection criteria used for polarization analysis (see Section 5.2). The temperature-sensitive modules, however, are far more susceptible to atmospheric contamination than the polarization modules. Thus, these cuts result in reduced efficiencies: 12.4%, 6.9%, and 6.8% for patches CMB-1, CMB-2, and CMB-3, respectively.[34] More tailoring of the cuts for these modules would improve efficiencies.

[34] Patch CMB-4 is excluded due to low data-selection efficiency and a lack of sufficient cross-linking.

In pipeline A, the analysis proceeds as described in Sections 5.1.3, 5.3.1, and 5.3.2 except for two aspects. First, in the TOD processing a second-order polynomial is fit and removed from each telescope half-scan instead of a linear function. This suppresses the increased contamination from atmospheric fluctuations in the temperature data. Second, we employ an iterative map maker based on the algorithm described by Wright et al. (1996). Map making for differential receivers requires that each pixel is measured at multiple array pointings or cross-linked. In order to improve cross-linking, we divide the temperature data into only four maps by azimuth and deck angle, rather than the 60 divisions used for polarization analysis. To calculate TE and TB power spectra, polarization maps are made for these four divisions, plus one additional map that contains all polarization data with pointings not represented in the temperature data.

For pipeline B, the algorithms for making temperature maps and estimating power spectra are identical to the polarization case, as described in Sections 5.3.3 and 5.3.4.

6. ANALYSIS VALIDATION

The QUIET data analysis follows a policy of not looking at the power spectra until the analysis is validated using a set of predefined tests for possible systematic effects.[35] The validation tests consist of a suite of null tests, comparisons across multiple analysis configurations, and consistency checks among power spectra from different CMB patches. Data-selection criteria, filtering methods, and the division of data into maps for cross-correlation in pipeline A are all evaluated based on the test results.

Details of tests found in this section describe pipeline A. While the pipeline-B analysis follows a similar program of null tests to verify the result, the increased computational requirements of the maximum-likelihood framework limit the number of tests that could be performed and require those tests to be run using lower-resolution maps than for the non-null analysis. The bulk of this section treats validation of the polarization analysis; at the end, we briefly describe the temperature analysis validation.

We conduct this validation in a blind-analysis framework to reduce experimenter bias, the influence of the experimenter's knowledge of prior results and theoretical predictions on the result (power spectra). Blind analysis, making the analysis choices without knowing the result, is a standard technique for minimizing this bias (Klein & Roodman 2005). In our blind-analysis framework, we finalize all aspects of the data analysis including calibration, data selection, and evaluation of the systematic error. Only after the analysis is finalized and the following validation tests pass do we examine the power spectra.

In a null test, the data are split into two subsets. Maps, m_1 and m_2, are made from each subset. The power spectra of the difference map, $m_{\mathrm{diff}} \equiv (m_1 - m_2)/2$, are analyzed for consistency with the hypothesis of zero signal. The null suite consists of 42 tests,[36] each targeting a possible source of signal contamination or miscalibration. These are highly independent tests; the data divisions for different null tests are correlated at only 8.8% on average. Nine tests divide the data by detector diode based on susceptibility to instrumental effects, such as instrumental polarization. Ten tests target effects that depend

[35] Some systematic effects, such as a uniform responsivity-calibration error, cannot be detected by these techniques, and are addressed in Section 8.

[36] Only 41 null tests are performed for patch CMB-4; one test is dropped because there are no data in one of the subsets.

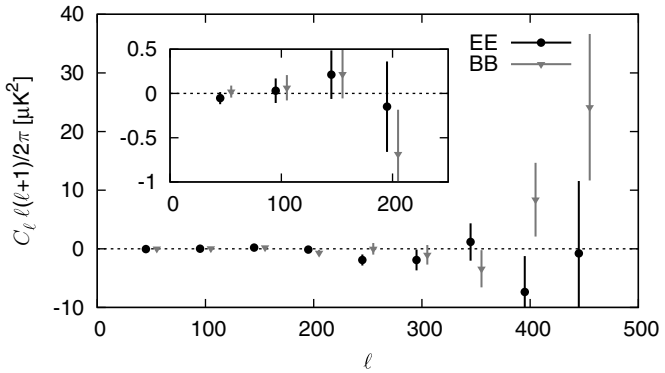

Figure 6. EE and BB power spectra for the patch CMB-1 null test between Q and U detector diodes. The inset shows the low-ℓ region in detail.

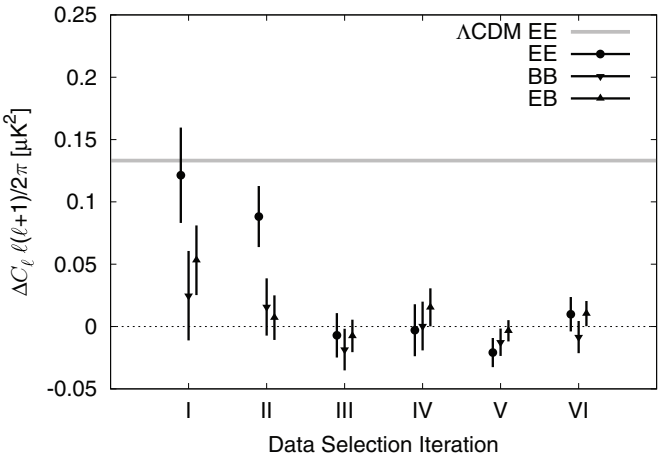

Figure 7. Power-spectra differences between the final data selection and six of the 32 earlier data-selection iterations, ordered by date. The lowest-ℓ bin of patch CMB-1 is shown. The error bars correspond to the expected fluctuations due to the differences in data selected, which are much smaller than the final statistical errors in this bin ($\approx 0.10\ \mu K^2$ for BB). Iterations that are closer to the final data selection have smaller errors. The expected EE power in this bin from the ΛCDM model is also shown for comparison.

on the telescope pointing such as data taken at high or low elevation. Five tests divide based on the proximity of the main or sidelobe beams to known sources such as the Sun and Moon. Eight tests target residual contamination in the TOD using statistics mentioned in Section 5.2. Ten tests divide the data by environmental conditions such as ambient temperature or humidity.

Each null test yields EE and BB power spectra in nine ℓ bins, calculated separately for each CMB patch. Figure 6 shows the power spectra from one null test. Although the EB spectra are also calculated for each null test, they are assigned lesser significance since sources of spurious EB power will also result in the failure of EE and BB null tests. Combining all EE and BB points for all patches and null tests in the null suite yields a total of 3006 null-spectrum points. For each power-spectrum bin b, we calculate the statistic $\chi_{\rm null} \equiv C_b^{\rm null}/\sigma_b$, where $C_b^{\rm null}$ is the null power and σ_b is the standard deviation of $C_b^{\rm null}$ in MC simulations. We evaluate both $\chi_{\rm null}$ and its square; $\chi_{\rm null}$ is sensitive to systematic biases in the null spectra while $\chi^2_{\rm null}$ is more responsive to outliers. We run MC simulations of the full null suite to take into account the small correlation among the null tests and the slight non-Gaussianity of the $\chi_{\rm null}$ distribution. Non-Gaussianity is caused by the small number of modes at low ℓ.

As we refine the data-selection criteria based on the results of the null suite, we use a second test to monitor changes in the non-null power spectra. Using a blind-analysis framework, we compute the difference of the power spectra between any two iterations of the data selection without revealing the non-null spectra. Furthermore, we randomize the sign of the difference to hide the direction of the change; knowledge of the direction could allow experimenter bias (e.g., a preference for low BB power). Figure 7 shows the differences in the power spectra between the final configuration and several intermediate iterations of the data selection, starting with data sets that showed significant failures for the null-test suite. Statistically significant differences indicate a change in the level of contamination in the selected data set. Our data-selection criteria are finalized when further iterations only result in statistically expected fluctuations. The sensitivity of this test is demonstrated by the fact that the expected fluctuations are much less than the statistical error of the final result.

Finally, the non-null power spectra are compared among the four CMB patches. A χ^2 statistic is computed from the deviation of each patch's non-null power spectra from the weighted average over all patches. The total χ^2 is compared to MC simulations to compute probabilities to exceed (PTE).

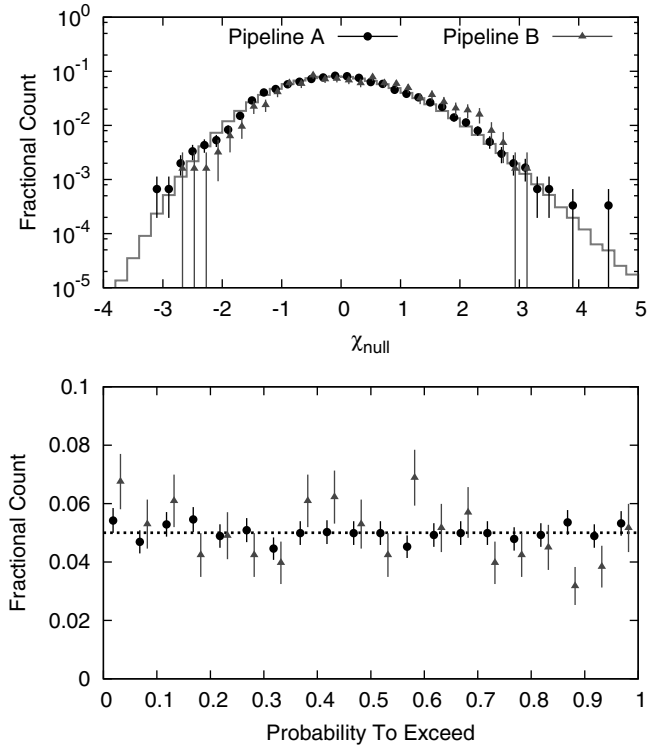

Figure 8. Null-suite statistics. The upper panel shows a histogram of the $\chi_{\rm null}$ values for the pipeline-A null suite (circles), pipeline-B null suite (triangles), and the average of 1024 MC realizations of the pipeline-A null suite (gray histogram). Both data and MC distributions show similar non-Gaussianity in the $\chi_{\rm null}$ statistic. The shift in $\chi_{\rm null}$ seen for pipeline B, also seen in earlier iterations of pipeline A, is discussed in the text. The lower panel shows a histogram of PTEs calculated from the $\chi^2_{\rm null}$ statistic (outliers from either side of the upper distribution manifest as low PTEs).

When all aspects of the analysis are finalized, the last round of null tests and CMB patch comparisons validates the non-null-power-spectra results. Figure 8 shows the distributions of the $\chi_{\rm null}$ statistic and of the PTEs corresponding to all $\chi^2_{\rm null}$ values from the full null suite. In pipeline A, the distribution of $\chi_{\rm null}$ is consistent with the expectation from MC simulations.

Table 4
Null-suite Probability to Exceed by Patch

Patch	Pipeline A (%)	Pipeline B (%)
CMB-1	44	7
CMB-2	19	43
CMB-3	16	23
CMB-4	68	28

Note. PTEs calculated from the sums of the $\chi^2_{\rm null}$ statistics, for EE and BB spectra points, over the null tests for each patch.

The mean of the $\chi_{\rm null}$ distribution is 0.02 ± 0.02; the mean of the MC-ensemble $\chi_{\rm null}$ distribution is also consistent with zero. The distribution of the $\chi^2_{\rm null}$ PTEs is uniform as expected. Table 4 lists the PTEs for the sums of the $\chi^2_{\rm null}$ statistic over all bins in each patch. Examinations of various subsets of the null suite, such as EE or BB only, do not reveal any anomalies. The EB null spectra do not indicate any failure either. Patch comparison PTEs are 0.16, 0.93, and 0.40 for EE, BB, and EB, respectively, demonstrating no statistically significant difference among the patches.

A similar, but smaller, null suite is run by pipeline B. Specifically, 21 null tests are made at a HEALPix resolution of $N_{\rm side} = 128$. The results obtained in these calculations are summarized in the bottom panel of Figure 8, and total PTEs for each patch are listed in Table 4. As in pipeline A, no anomalous values are found.

Finally, we make a comment on the usefulness of the $\chi_{\rm null}$ distribution (as opposed to the $\chi^2_{\rm null}$ distribution) for identifying and quantifying potential contaminants. During the blind stage of the analysis, a positive bias in the $\chi_{\rm null}$ distribution of 0.21 (0.19) was identified using pipeline A (B) (corresponding to 21% (19%) of the statistical errors). The number from pipeline A was obtained when including autocorrelations in its power-spectra estimator. When excluding autocorrelations, and cross-correlating maps made from data divided by time (day by day), the bias decreased to 0.10. Further detailed studies lead to the division of data into maps based on the telescope pointing, as described in Section 5.3; the result is an elimination of the observed bias.

The maximum-likelihood technique employed by pipeline B intrinsically uses autocorrelations, and a corresponding shift in the $\chi_{\rm null}$ distribution is seen in Figure 8. However, as will be seen in Section 7, the power spectra from the two pipelines are in excellent agreement, thereby confirming that any systematic bias coming from including autocorrelations is well below the level of the statistical errors. We close this section by mentioning that we know of no other CMB experiment reporting an examination of the $\chi_{\rm null}$ distribution, which is sensitive to problems not detected by examining the $\chi^2_{\rm null}$ distribution only.

6.1. Validation of the Temperature Analysis

A smaller number of null tests is used for the temperature analysis. Several are not applicable and others are discarded due to lack of data with sufficient cross-linking. Even so, we are able to run suites of 29, 27, and 23 TT null tests on patches CMB-1, CMB-2, and CMB-3, respectively. We calculate the sums of $\chi^2_{\rm null}$ statistics, yielding PTEs of 0.26 and 0.11 for patches CMB-1 and CMB-2, respectively. No significant outliers are found for these patches. However, a 5σ outlier in a single test[37] is found in patch CMB-3, implying contamination in its temperature map. CMB-3 is therefore excluded from further analysis. We confirm consistency between the patches CMB-1 and CMB-2 with a PTE of 0.26.

With no significant contamination in TT, EE, or BB spectra, one may be confident that the TE and TB spectra are similarly clean. For confirmation, we calculate TE and TB null spectra for the five null tests that are common to the temperature and polarization analyses. These yield PTEs of 0.61 and 0.82 for TE, and 0.16 and 0.55 for TB, for patches CMB-1 and CMB-2, respectively, with no significant outliers. Patch consistency checks give PTEs of 0.48 for TE and 0.26 for TB. Thus, the TE and TB power spectra, as well as the TT, pass all validation tests that are performed.

Table 5
CMB-Spectra Band Powers from QUIET Q-band Data

ℓ bin	EE	BB	EB
25–75	$0.33^{+0.16}_{-0.11}$ [a]	$-0.01^{+0.06}_{-0.04}$	$0.00^{+0.07}_{-0.07}$
76–125	$0.82^{+0.23}_{-0.20}$	$0.04^{+0.14}_{-0.12}$	$-0.10^{+0.11}_{-0.12}$
126–175	$0.93^{+0.34}_{-0.31}$	$0.24^{+0.28}_{-0.25}$	$0.71^{+0.22}_{-0.20}$
176–225	$1.11^{+0.58}_{-0.52}$	$0.64^{+0.53}_{-0.46}$	$0.18^{+0.38}_{-0.38}$
226–275	$2.46^{+1.10}_{-0.99}$	$1.07^{+0.98}_{-0.86}$	$-0.52^{+0.68}_{-0.69}$
276–325	$8.2^{+2.1}_{-1.9}$	$0.8^{+1.6}_{-1.4}$	$0.9^{+1.3}_{-1.3}$
326–375	$11.5^{+3.6}_{-3.3}$	$-2.2^{+2.7}_{-2.4}$	$0.0^{+2.0}_{-2.0}$
376–425	$15.0^{+6.2}_{-5.8}$	$-4.9^{+5.3}_{-4.9}$	$3.2^{+3.9}_{-3.9}$
426–475	21^{+13}_{-11}	2^{+11}_{-10}	$4.5^{+8.3}_{-8.2}$

Notes. Units are thermodynamic temperatures, μK^2, scaled as $C_\ell \ell(\ell+1)/2\pi$.
[a] Patch CMB-1 has significant foreground contamination in the first EE bin.

7. RESULTS

We report results from the first season of QUIET Q-band observations: CMB power spectra, derived foreground estimates, and constraints on the tensor-to-scalar ratio, r.

7.1. Polarization Power Spectra

The CMB power spectra are reported in nine equally spaced bands with $\Delta\ell = 50$, beginning at $\ell_{\rm min} = 25$. Given the patch size, modes with $\ell < \ell_{\rm min}$ cannot be measured reliably. The correlation between neighboring bins is typically -0.1; it becomes negligible for bins further apart.

The EE, BB, and EB polarization power spectra estimated by both pipelines are shown in Figure 9. The agreement between the results obtained by the two pipelines is excellent, and both are consistent with the ΛCDM concordance cosmology. Our findings and conclusions are thus fully supported by both pipelines. Only the statistical uncertainties are shown here; we treat systematic errors in Section 8. Because the systematic error analysis was only done for pipeline A, we adopt its power-spectra results (tabulated in Table 5) as the official QUIET results.

The bottom sub-panels in Figure 9 show the window and transfer functions for each bin computed by pipeline A. Figure 10 shows the maps for patch CMB-1 computed by pipeline B, and Figure 11 shows the QUIET power spectra in comparison with the most relevant experiments in our

[37] This null test divides the data based on array pointing.

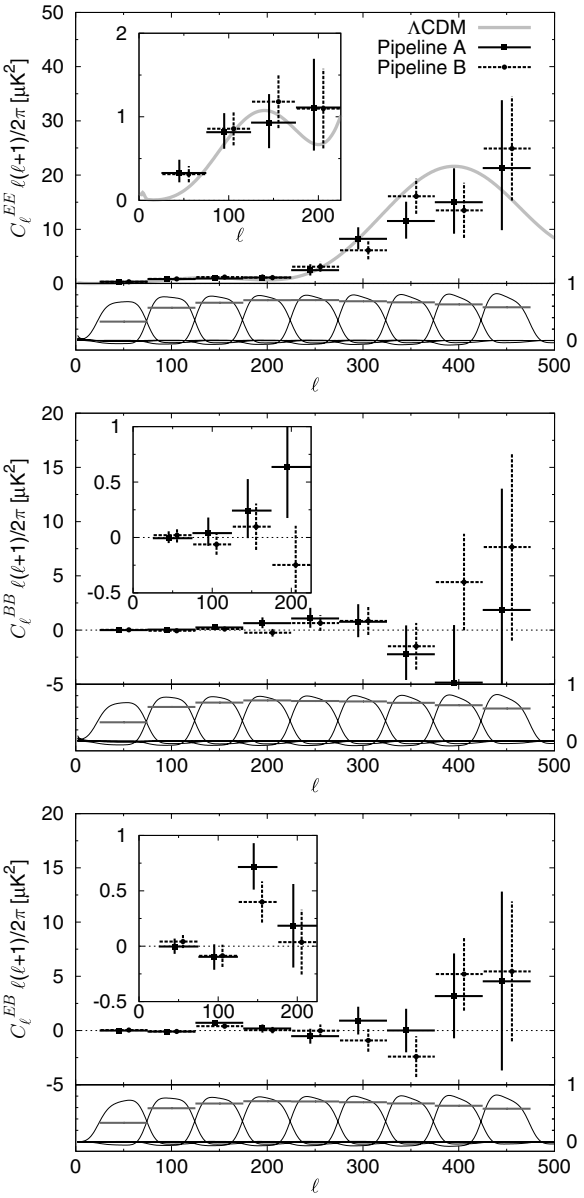

Figure 9. EE, BB, and EB power spectra from each QUIET pipeline, all four patches combined. The insets show the low-ℓ region in detail. Window and transfer functions for each ℓ bin are shown below the corresponding power spectra in black and gray, respectively. The window function combines the mode-mode-coupling kernel $M_{\ell\ell'}$ with the beam (B_ℓ) and represents, in combination with the transfer function (F_ℓ), the response in each band to the true C_ℓ spectrum. The EE point in the lowest-ℓ bin includes foreground contamination from patch CMB-1. For this display, pipeline A shows frequentist 68% confidence intervals while pipeline B uses the diagonal elements of the Fisher matrix; the difference is most pronounced in the lowest-ℓ bin where the likelihood is the most non-Gaussian.

multipole range.[38] Additional plots and data files are available at the QUIET Web site at the University of Chicago.[39]

Fitting only a free amplitude, q, to the EE spectrum[40] relative to the seven-year best-fit *WMAP* ΛCDM spectrum (Larson et al. 2011), we find $q = 0.87 \pm 0.10$ for pipeline A and

[38] Since Larson et al. (2011) do not provide an upper limit on the BB power, we use the diagonal elements of the Fisher matrix and show the points that are 1.65 σ above their central values as 95% upper limits.

[39] http://quiet.uchicago.edu/results/index.html

[40] Only $\ell \geqslant 76$ are used in the EE fit and the χ^2 calculation relative to ΛCDM because the first EE bin has a significant foreground contribution (see Section 7.2).

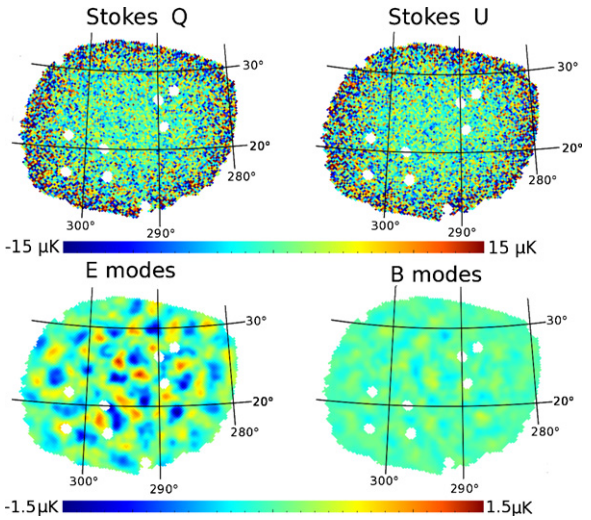

Figure 10. Maps of patch CMB-1 in Galactic coordinates. The top row shows our polarization maps with compact sources masked (white disks). The bottom row shows E and B modes decomposed using a generalized Wiener filter technique, implemented through Gibbs sampling where the signal term of the Wiener filter is marginalized over the power spectra constrained by the data of this patch themselves (Eriksen et al. 2004; Larson et al. 2007). The maps include only modes for $\ell \geqslant 76$ and smoothed to 1° FWHM; lower multipoles are removed due to a significant foreground contribution. Note the clear difference in amplitude: the E modes show a high-signal-to-noise cosmological signal while the B modes are consistent with noise. Maps for the other patches are available online.

(A color, extended version of this figure is available in the online journal.)

$q = 0.94 \pm 0.09$ for pipeline B. Taking into account the full non-Gaussian shapes of the likelihood functions, both results correspond to more than a 10σ detection of EE power. In particular, in the region of the first peak, $76 \leqslant \ell \leqslant 175$, we detect EE polarization with more than 6σ significance, confirming the only other detection of this peak made by BICEP at higher frequencies. The χ^2 relative to the ΛCDM model, with $C_\ell^{EB} = C_\ell^{BB} = 0$, is 31.6 (24.3) with 24 degrees of freedom, corresponding to a PTE of 14% (45%) for pipeline A (B).

7.2. Foreground Analysis

In order to minimize possible foreground contamination, QUIET's four CMB patches were chosen to be far from the Galactic plane and known Galactic synchrotron spurs. In these regions, contributions from thermal dust emission are negligible in Q band. Spinning dust is expected to be polarized at no more than a few percent in Q band (Battistelli et al. 2006; Lopez-Caraballo et al. 2011), so we expect the contribution to polarized foreground emission in our patches to be small. We therefore consider only two dominant sources of possible foreground contamination, namely, compact radio sources and Galactic diffuse synchrotron emission.

To limit the effect of compact radio sources, we apply a compact-source mask to our maps before computing the power spectra, as described in Section 5. We also evaluate the CMB spectra both with and without the full *WMAP* temperature compact-source mask (Gold et al. 2011), and find no statistically significant changes. The possible contribution from compact radio sources with fluxes below the *WMAP* detection level (1 Jy) is small: 0.003 μK^2 at $\ell = 50$ and 0.01 μK^2 at $\ell = 100$ (Battye et al. 2011).[41] We therefore conclude that our results are robust

[41] The estimate is robust since 90% of the contribution comes from the high-flux population between 100 mJy and 1 Jy, where the distribution of the population is well understood.

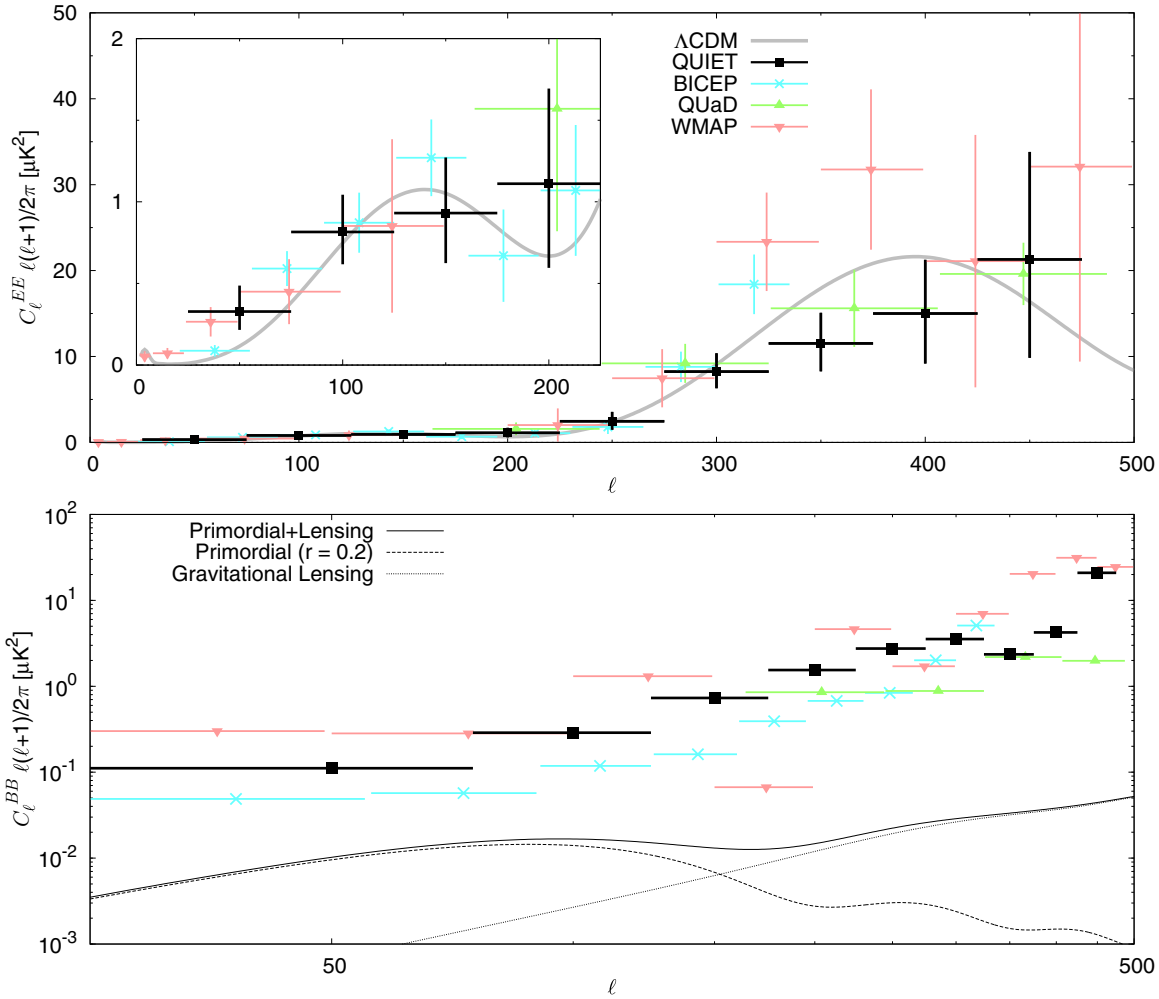

Figure 11. Top panel shows EE results with 68% C.L. error bars; the bottom panel shows BB 95% C.L. upper limits. For comparison, we also plot results from previous experiments (Brown et al. 2009; Chiang et al. 2010; Larson et al. 2011) and the ΛCDM model (the value $r = 0.2$ is currently the best 95% C.L. limit on tensor modes).

(A color version of this figure is available in the online journal.)

with respect to contamination from compact radio sources and that the dominant foreground contribution comes from diffuse synchrotron emission.

In Figure 12, we show the power spectra measured from each patch. The CMB-1 EE band power for the first bin is $0.55 \pm 0.14\,\mu\mathrm{K}^2$, a 3σ outlier relative to the expected ΛCDM band power of $0.13\,\mu\mathrm{K}^2$; while not significant enough to spoil the overall agreement among the patches as shown in Section 6, this is a candidate for a bin with foreground contamination.

To estimate the Q-band polarized synchrotron contamination in our CMB patches, we process the *WMAP*7 K-band (23 GHz) map through pipeline A and estimate its band power, $\hat{C}_b^{\mathrm{KK}}$, as well as the cross-spectra with the QUIET Q-band data, $\hat{C}_b^{\mathrm{QK}}$. These results are shown for the first bin ($25 \leqslant \ell \leqslant 75$; $b = 1$) in Table 6, together with the corresponding QUIET band powers, $\hat{C}_b^{\mathrm{QQ}}$. Since foregrounds do not contribute to the sample variance, the uncertainties for $\hat{C}_{b=1}^{\mathrm{KK}}$ and $\hat{C}_{b=1}^{\mathrm{QK}}$ are given by instrumental noise only, including contributions from both *WMAP* and QUIET. For $\hat{C}_{b=1}^{\mathrm{QQ}}$, sample variance as predicted by the ΛCDM model is also included.

There is significant EE power in patch CMB-1 as measured by $\hat{C}_{b=1}^{\mathrm{KK}}$. We also find a correspondingly significant

Table 6
Band and Cross Powers for $\ell = 25$–75

Patch	Spectrum	$\hat{C}_{b=1}^{\mathrm{KK}}$	$\hat{C}_{b=1}^{\mathrm{QK}}$	$\hat{C}_{b=1}^{\mathrm{QQ}}$
CMB-1	EE	$\mathbf{17.4 \pm 4.7}$	$\mathbf{3.30 \pm 0.55}$	$\mathbf{0.55 \pm 0.14}$
	BB	4.8 ± 4.5	0.40 ± 0.41	0.06 ± 0.08
	EB	-6.2 ± 3.2	0.27 ± 0.38	0.10 ± 0.08
CMB-2	EE	5.5 ± 3.7	0.01 ± 0.56	0.23 ± 0.19
	BB	4.6 ± 3.4	0.18 ± 0.48	-0.11 ± 0.13
	EB	-5.5 ± 2.8	-0.39 ± 0.41	-0.20 ± 0.12
CMB-3	EE	0.2 ± 1.9	0.64 ± 0.43	0.10 ± 0.18
	BB	-0.3 ± 2.6	0.33 ± 0.35	0.01 ± 0.13
	EB	1.4 ± 1.7	-0.34 ± 0.30	$\mathbf{-0.27 \pm 0.11}$
CMB-4	EE	-5.2 ± 5.1	0.7 ± 1.2	0.65 ± 0.58
	BB	-2.6 ± 5.2	-0.1 ± 1.1	-0.37 ± 0.52
	EB	-1.0 ± 3.9	0.0 ± 0.9	-0.15 ± 0.47

Notes. Power-spectra estimates for the first multipole bin for each patch, computed from the *WMAP*7 K-band data and the QUIET Q-band data. The units are $\ell(\ell+1)C_\ell/2\pi(\mu\mathrm{K}^2)$ in thermodynamic temperature. Uncertainties for $\hat{C}_{b=1}^{\mathrm{KK}}$ and $\hat{C}_{b=1}^{\mathrm{QK}}$ include noise only. For $\hat{C}_{b=1}^{\mathrm{QQ}}$, they additionally include CMB sample variance as predicted by ΛCDM. Values in bold are more than 2σ away from zero.

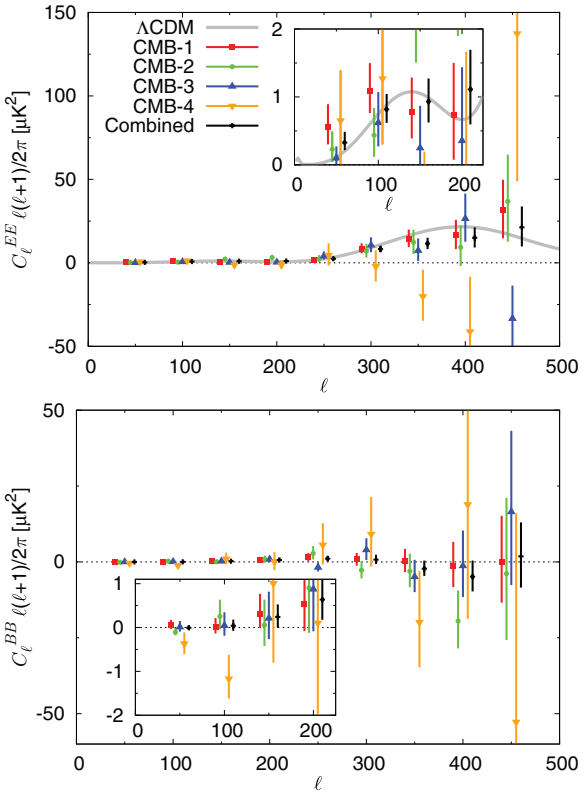

Figure 12. CMB power spectra are shown for each patch individually. The top and bottom panels show the EE and BB spectra, respectively. The different error bars for each patch mainly reflect the amounts of time each was observed.
(A color version of this figure is available in the online journal.)

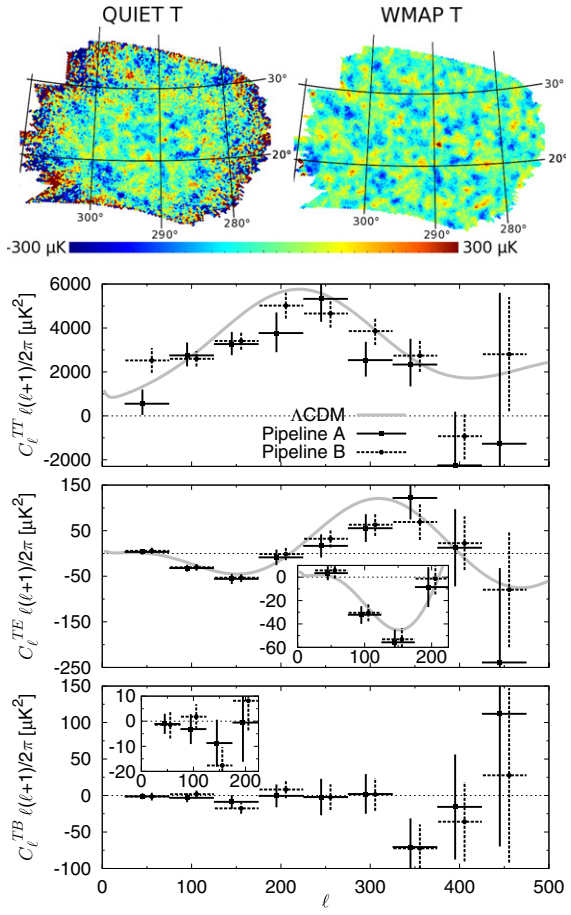

Figure 13. Top row compares our temperature map to the *WMAP* seven-year *Q*-band map (Jarosik et al. 2010) for patch CMB-1 in Galactic coordinates. Lower panels show the CMB temperature power spectra: TT, TE, and TB.
(A color version of this figure is available in the online journal.)

cross-correlation between the *WMAP K* band and the QUIET *Q* band, confirming that this excess power is not due to systematic effects in either experiment and is very likely a foreground. No significant power is found in any other case. The non-detection of foreground power at $\ell > 75$ is consistent with the expected foreground dependence: $\propto \ell^{-2.5}$ (Carretti et al. 2010), and the low power found in $\hat{C}_{b=1}^{\rm KK}$.

The excess power observed in the first EE bin of CMB-1 is fully consistent with a typical synchrotron frequency spectrum. To see this, we extrapolate $\hat{C}_{b=1}^{\rm KK}$ from *K* band to *Q* band, assuming a spectral index of $\beta = -3.1$ (Dunkley et al. 2009), and calculate the expected power in $C_{b=1}^{\rm QK}$ and $C_{b=1}^{\rm QQ}$,

$$C_{b=1}^{\rm QK} = \frac{1.05}{1.01}\left(\frac{43.1}{23}\right)^{\beta}\hat{C}_{b=1}^{\rm KK} = 2.57 \pm 0.69\,\mu{\rm K}^2\,, \quad (8)$$

$$C_{b=1}^{\rm QQ} = \left[\frac{1.05}{1.01}\left(\frac{43.1}{23}\right)^{\beta}\right]^2\hat{C}_{b=1}^{\rm KK} = 0.38 \pm 0.10\,\mu{\rm K}^2\,, \quad (9)$$

where the prefactor accounts for the fact that β is defined in units of antenna temperature, and the uncertainties are scaled from that of $\hat{C}_{b=1}^{\rm KK}$. These predictions are fully consistent with the observed values of $\hat{C}_{b=1}^{\rm QK}$ and $\hat{C}_{b=1}^{\rm QQ}$, when combined with the ΛCDM-expected power. We conclude that the excess power is indeed due to synchrotron emission.

7.3. Constraints on Primordial B Modes

We constrain the tensor-to-scalar ratio, *r*, using the QUIET measurement of the BB power spectrum at low multipoles ($25 \leqslant \ell \leqslant 175$). Here, *r* is defined as the ratio of the primordial-gravitational-wave amplitude to the curvature-perturbation amplitude at a scale $k_0 = 0.002\ {\rm Mpc}^{-1}$. We then fit our measurement to a BB-spectrum template computed from the ΛCDM concordance parameters with *r* allowed to vary. For simplicity, we fix the tensor spectral index at $n_t = 0$ in computing the template.[42] This choice makes the BB-power-spectrum amplitude directly proportional to *r*.

For pipeline A, we find $r = 0.35^{+1.06}_{-0.87}$, corresponding to $r < 2.2$ at 95% confidence. Pipeline B obtains $r = 0.52^{+0.97}_{-0.81}$. The results are consistent; the lower panel of Figure 11 shows our limits on BB power in comparison with those from BICEP, QUaD, and *WMAP*. QUIET lies between BICEP and *WMAP* in significantly limiting *r* from measurements of CMB-B-mode power in our multipole range. Although we neither expected nor detected any BB foreground power, the detection of an EE foreground in patch CMB-1 suggests that BB foregrounds might be present at a smaller level. We emphasize that the upper limit we report is therefore conservative.

7.4. Temperature Power Spectra

Figure 13 compares the QUIET and *WMAP Q*-band temperature maps and TT, TE, and TB power spectra. Agreement with the ΛCDM model is good. This is a strong demonstration of the raw sensitivity of the QUIET detectors; the single QUIET

[42] Our definition of *r* agrees with Chiang et al. (2010).

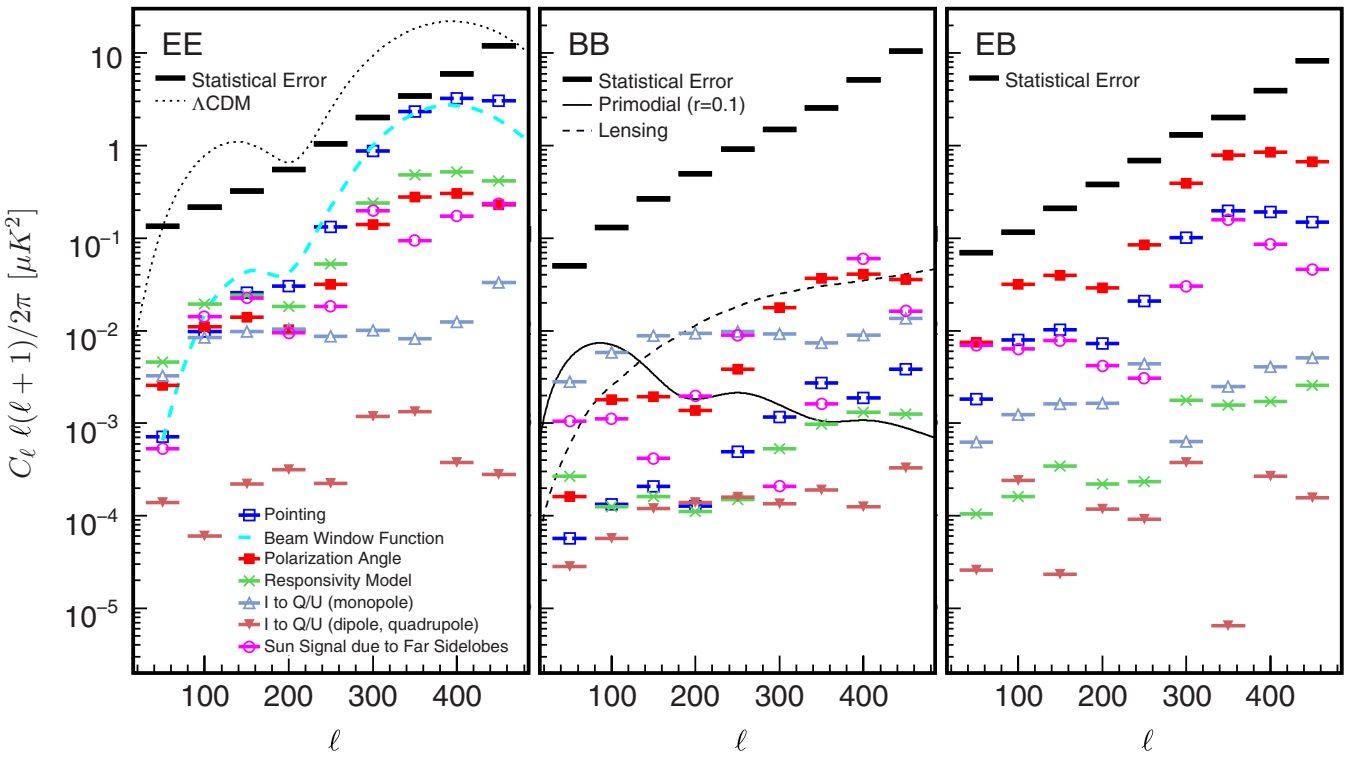

Figure 14. Systematic uncertainty estimates for EE, BB, and EB power spectra. Estimates for a variety of effects (see the text) are shown for the three power spectra. In all cases, they are well below the statistical errors, which are also shown. In particular, the contaminations to the primordial-B-mode signal, at multipoles below 100, are below the level of $r = 0.1$, even though we do not make a correction for the largest contaminant, the monopole leakage.

(A color version of this figure is available in the online journal.)

differential-temperature assembly produces a high-signal-to-noise map using only 189 hr (after selection) of observations. The high sensitivity of these modules makes them very useful for calibration, pointing estimation, and consistency checks (see Section 4).

8. SYSTEMATIC ERRORS

The passing of the null suite itself limits systematic uncertainty, but to get well below the statistical errors, dedicated studies are needed. They are important for gaining confidence in the result and also for evaluating the potential of the methods and techniques we use for future efforts. We pay special attention to effects that can generate false B-mode signals. Our methodology is to simulate and then propagate calibration uncertainties (see Section 4) and other systematic effects through the entire pipeline. The systematic errors in the power spectra are shown in Figure 14. The possible contaminations are well below the statistical errors; in particular, the levels of spurious B modes are less than the signal of $r = 0.1$. This is the lowest level of BB contamination yet reported by any CMB experiment. This section describes how each effect in Figure 14 is determined and considers three additional possible sources of contamination.

An uncertainty not shown in Figure 14 is that arising from the overall responsivity error estimate of 6% (12% in power-spectra units). After including the effect of possible time-dependent responsivity variations (4%, see below), the power-spectra uncertainty is 13%. It is multiplicative, affecting all power-spectra results independent of multipole.

8.1. Beam Window Function and Pointing

The uncertainty in the beam window function is another multiplicative factor, one which increases with multipole. We estimate this uncertainty using the difference of the beam window functions measured for the central module and the modules of the differential-temperature assembly, which are at the edge of the array. The difference is statistically significant, coming from the different locations (with respect to the optics) in the focal plane; it is expected from the pre-season antenna range measurements.

Uncertainties in pointing lead to distortions in polarization maps. E power will be underestimated and spurious B power (if the distortions are nonlinear) generated (Hu et al. 2003). We quantify these effects by using the differences in pointing solutions from two independent models: the fiducial model used for the analysis and an alternative model based on a different set of calibrating observations. We also modeled and included the effects of the deck-angle-encoder shift which occurred for a portion of the season (Section 4.3).

8.2. Responsivity and Polarization Angle

Responsivity shifts, particularly within CESs, lead to distortions in the maps. Full-pipeline simulations quantify the shifts caused by variations in the cryostat or electronics temperatures. Similarly shifts from using responsivities determined from the Moon data, Tau A data, or from the sparse wire grid, rather than those from the sky dips, are determined. We also incorporate the uncertainty in the atmospheric-temperature model used in analyzing the sky-dip data. The largest possible effects on the power spectra are shown in Figure 14.

Uncertainties in the orientation of the polarization axes of the modules can lead to leakage between E and B modes. To quantify this leakage, we use the differences in power spectra where these angles are determined from Moon data, Tau A data, and the sparse-wire-grid data. As expected, the largest effects

show up in EB power. We also estimate systematic error due to possible fluctuation of the detector angles over the course of the season. The contribution is negligibly small compared to the overall shift of the angles described above. Both effects are included in the "Polarization Angle" points in Figure 14.

8.3. Instrumental Polarization

As described in Section 4.5, the I to Q (U) leakage coefficients for the QUIET detector diodes are small: 1% (0.2%). Except in the case of patch CMB-4, our scanning strategy significantly reduces this effect with the combination of sky and deck-angle rotation.

We estimate spurious Q and U in the maps for each CES-diode using the *WMAP* temperature map and our known leakages. Shown in Figure 14 are the estimates of spurious EE, BB, and EB powers from full-pipeline simulations, where for each realization the spurious Q and U are added to the Q and U from simulated ΛCDM E modes. While this method has an advantage of being able to use the real (not simulated) temperature map, it does not incorporate TE correlation, which only affects the spurious EE power. As a complement, we repeat the study, but using simulated ΛCDM maps for both temperature and polarization; this only changes the estimate of spurious EE power by 30% at most. Because the spurious power is as small as it is, we have treated it as a systematic rather than correcting for it. Doing so would give us a further order of magnitude suppression.

Differing beam ellipticities can also induce higher multipole polarization signals. We measure these leakages from Tau A and Jupiter observations and find that the higher-order multipoles are at most 0.1% of the main-beam peak amplitude. The corresponding effects on the power spectra, which are seen in Figure 14, are of little concern.

8.4. Far Sidelobes Seeing the Sun

While we make cuts to reduce the effects of far sidelobes seeing the Sun (Sections 2 and 5.1.3), small contaminations could remain. We make full-season maps for each diode in Sun-centered coordinates and then use these maps to add contamination to full-pipeline CMB simulations. The excess power found in the simulations is taken as the systematic uncertainty. We do not observe any signature from the Moon, nor do we cut on proximity to it. We estimate the related systematic error and find that it is negligibly small compared to that assigned to the contamination from the Sun.

8.5. Other Possible Sources of Systematic Uncertainty

Here, we discuss a few additional potential sources of systematic uncertainty, which are found to be subdominant.

Ground-synchronous signals. QUIET's far sidelobes do see the ground for some diodes at particular elevations and deck angles. Ground pickup that is constant throughout a CES is removed by our TOD filters; the net effect of this filtering in the full-season maps is a correction of $\approx 1\ \mu$K.

The only concern is ground pickup that changes over the short span of a single CES. We find little evidence for changes even over the entire season, let alone over a single CES. We therefore conservatively place an upper limit on such changes using the statistical errors on the ground-synchronous signal. We start with the CES and module with the largest ground pickup. We then simulate one day's worth of data, inserting a ground-synchronous signal that changes by its statistical error. Given the distribution in the magnitude of the ground-synchronous signal and assuming that changes in this signal are proportional to the size of the signal itself, by considering that the signals from changing pickup add incoherently into the maps made from multiple CES-diodes at a variety of elevations and deck angles, we estimate an upper limit on residual B power from possible changing ground-pickup signals. The result is $\lesssim 10^{-4}\ \mu\mathrm{K}^2$ at multipoles below 100.

ADC nonlinearities. The possible residual after the correction for the nonlinearity in the ADC system results in effects similar to the I to Q (or U) leakage and the variation of the responsivity during the CES. We estimate such effects based on the uncertainty in the correction parameters, confirming that there is at most a 3% additional effect for the leakage bias, and that the responsivity effect is also small, less than half of the systematic error shown for the responsivity in Figure 14.

Data-selection biases. Cuts can cause biases if they are, for example, too stringent. We expect none but to be sure we apply our selection criteria to 144 CMB + noise simulations. No bias is seen, and in particular we limit any possible spurious B modes from this source to $\lesssim 10^{-3}\ \mu\mathrm{K}^2$ at multipoles below 100.

9. CONCLUSIONS

QUIET detects polarization in the EE power spectrum at 43 GHz. We confirm with high significance the detection of polarization in the region of the first acoustic peak (Chiang et al. 2010) in the multipole region $\ell = 76$–175. We find no significant power in either BB or EB between $\ell = 25$ and $\ell = 475$. We measure the tensor-to-scalar ratio to be $r = 0.35^{+1.06}_{-0.87}$.

These results are supported by a very extensive suite of null tests in which 42 divisions of data were used for each of 33 different cut configurations. The selection criteria and systematic errors were determined before the power spectra themselves were examined. Biases were revealed during this process, the last of which was a contamination present in the null spectra at the level of about 20% of the statistical errors, but eliminated when cross-correlating maps with differing telescope pointings. The robustness of the final results is further supported by having two pipelines with results in excellent agreement, even though one uses only cross-correlations while the other also uses autocorrelations.

Several possible systematic effects are studied with full end-to-end simulations. The possible contaminations in the B-mode power are thereby limited to a level smaller than for any other published experiment: below the level of $r = 0.1$ for the primordial B modes; simply correcting for the known level of instrumental polarization would reduce this to $r < 0.03$. This very low level of systematic uncertainty comes from the combination of several important design features, including a new time-stream "double-demodulation" technique, side-fed Dragonian optics, natural sky rotation, and frequent deck rotation.

The correlation modules we use have a polarization sensitivity (Q and U combined) of 280 $\mu\mathrm{K}\sqrt{\mathrm{s}}$, leading to an array sensitivity of 69 $\mu\mathrm{K}\sqrt{\mathrm{s}}$. Further, the $1/f$ noise observed in our detectors is small: the median knee frequency is just 5.5 mHz. One important outcome of this work, then, is the demonstration that our detectors, observing from a mid-latitude site, give excellent sensitivity and systematic immunity.

Because of our mid-latitude site, we are driven to collect data in four separate patches. While we lose some sensitivity (compared to going deeper on a single patch), there are a few advantages that we have exploited. The patches are scanned differently, in terms of time of day and the degree of

cross-linking, and these differences allow some important systematic checks. Another advantage concerns foregrounds.

Foreground contamination is expected to be one of the main limiting factors in the search for primordial B modes. Indeed we report a 3σ detection of synchrotron emission in one of our four CMB patches, originally chosen for their expected low foreground levels. Our detection is only in EE; our BB 2σ limit permits a BB signal about half as large. If we extrapolate that value to the foreground minimum of about 94 GHz, we would have synchrotron contamination at the level of $r = 0.05$ from this one patch. Neither *WMAP* nor *Planck* will have enough sensitivity (Tauber et al. 2010) to sufficiently constrain the polarized synchrotron amplitude at this level in any patch. In fact, our *Q*-band polarization maps are already as deep or deeper than what *Planck* will achieve at the same frequency. Dedicated low-frequency observations are clearly needed to achieve such constraints. When foreground cleaning becomes important, consistency among separate patches will be an important handle on our understanding.

Further progress must be made through larger arrays and longer integration times. In hand, we have data collected by the 90 element *W*-band array with similar sensitivity to our *Q*-band array and more than twice the number of observing hours. Results from the analysis of that data set will be reported in future publications. A *W*-band receiver with the sensitivity to reach below the level of $r = 0.01$ is under development.

Support for the QUIET instrument and operation comes through the NSF cooperative agreement AST-0506648. Support was also provided by NSF awards PHY-0355328, AST-0448909, AST-1010016, and PHY-0551142; KAKENHI 20244041, 20740158, and 21111002; PRODEX C90284; a KIPAC Enterprise grant; and by the Strategic Alliance for the Implementation of New Technologies (SAINT).

Some work was performed on the Joint Fermilab-KICP Supercomputing Cluster, supported by grants from Fermilab, the Kavli Institute for Cosmological Physics, and the University of Chicago. Some work was performed on the Titan Cluster, owned and maintained by the University of Oslo and NOTUR (the Norwegian High Performance Computing Consortium), and on the Central Computing System, owned and operated by the Computing Research Center at KEK. Portions of this work were performed at the Jet Propulsion Laboratory (JPL) and California Institute of Technology, operating under a contract with the National Aeronautics and Space Administration. The *Q*-band polarimeter modules were developed using funding from the JPL R&TD program.

C.D. acknowledges an STFC Advanced Fellowship and an ERC IRG grant under FP7. P.G.F. and J.A.Z. gratefully acknowledge the support of the Beecroft Institute of Particle Astrophysics and Cosmology, the Oxford Martin School, and the Science and Technology Facilities Council. L.B., R.B., and J.M. acknowledge support from CONICYT project Basal PFB-06. R.B. acknowledges support from ALMA-Conicyt 31080022 and 31070015. A.D.M. acknowledges a Sloan foundation fellowship.

PWV measurements were provided by the Atacama Pathfinder Experiment (APEX). We thank CONICYT for granting permission to operate within the Chajnantor Scientific Preserve in Chile, and ALMA for providing site infrastructure support. Field operations were based at the Don Esteban facility run by Astro-Norte. We are particularly indebted to the engineers and technician who maintained and operated the telescope: José Cortés, Cristobal Jara, Freddy Muñoz, and Carlos Verdugo.

In addition, we acknowledge the following people for their assistance in the instrument design, construction, commissioning, operation, and in data analysis: Augusto Gutierrez Aitken, Colin Baines, Phil Bannister, Hannah Barker, Matthew R. Becker, Alex Blein, Mircea Bogdan, April Campbell, Anushya Chandra, Sea Moon Cho, Emma Curry, Maire Daly, Richard Davis, Fritz Dejongh, Joy Didier, Greg Dooley, Hans Eide, Will Grainger, Jonathon Goh, Peter Hamlington, Takeo Higuchi, Seth Hillbrand, Christian Holler, Ben Hooberman, Kathryn D. Huff, William Imbriale, Koji Ishidoshiro, Eiichiro Komatsu, Jostein Kristiansen, Richard Lai, Erik Leitch, Kelly Lepo, Martha Malin, Mark McCulloch, Oliver Montes, David Moore, Makoto Nagai, Ian O'Dwyer, Stephen Osborne, Stephen Padin, Felipe Pedreros, Ashley Perko, Alan Robinson, Jacklyn Sanders, Dale Sanford, Mary Soria, Alex Sugarbaker, David Sutton, Matias Vidal, Liza Volkova, Edward Wollack, Stephanie Xenos, and Mark Zaskowski.

REFERENCES

Battistelli, E. S., Rebolo, R., Rubiño-Martín, J. A., et al. 2006, ApJ, 645, L141
Battye, R. A., Browne, I. W. A., Peel, M. W., Jackson, N. J., & Dickinson, C. 2011, MNRAS, 413, 132
Bischoff, C., Hyatt, L., McMahon, J. J., et al. 2008, ApJ, 684, 771
Bond, J. R., Jaffe, A. H., & Knox, L. 1998, Phys. Rev. D, 57, 2117
Bornemann, J., & Labay, V. A. 1995, IEEE Trans. MTT, 43, 95
Brown, M. L., Ade, P., Bock, J., et al. 2009, ApJ, 705, 978
Buder, I. 2010, Proc. SPIE, 7741, 77411D
Carretti, E., Haverkorn, M., McConnell, D., et al. 2010, MNRAS, 405, 1670
Challinor, A., & Chon, G. 2005, MNRAS, 360, 509
Chang, S., & Prata, A. 2004, IEEE Trans. Antennas Propag., 52, 12
Chiang, H. C., Ade, P. A. R., Barkats, D., et al. 2010, ApJ, 711, 1123
Dragone, C. 1978, Bell Syst. Tech. J., 57, 2663
Dumoulin, R. N. 2010, Proc. SPIE, 7741, 77412N
Dunkley, J., Spergel, D. N., Komatsu, E., et al. 2009, ApJ, 701, 1804
Eriksen, H. K., O'Dwyer, I. J., Jewell, J. B., et al. 2004, ApJS, 155, 227
Feldman, H. A., Kaiser, N., & Peacock, J. A. 1994, ApJ, 426, 23
Gold, B., Odegard, N., Weiland, J. L., et al. 2011, ApJS, 192, 15
Gorski, K. M., Hivon, E., Banday, A. J., et al. 2005, ApJ, 622, 759
Gundersen, J., & Wollack, E. 2009, J. Phys.: Conf. Ser., 155, 012005
Güsten, R., Nyman, L. Å., Schilke, P., et al. 2006, A&A, 454, L13
Hafez, Y., Davies, R. D., Davis, R. J., et al. 2008, MNRAS, 388, 1775
Hamimeche, S., & Lewis, A. 2008, Phys. Rev. D, 77, 103013
Hansen, F. K., & Gorski, K. M. 2003, MNRAS, 343, 559
Hivon, E., Gorski, K. M., Netterfield, C. B., et al. 2002, ApJ, 567, 2
Hu, W., Hedman, M., & Zaldarriaga, M. 2003, Phys. Rev. D, 67, 043004
Imbriale, W. A., Gundersen, J., & Thompson, K. L. 2011, IEEE Trans. Antennas Propag., 59, 1972
Jarosik, N., Bennett, C. L., Dunkley, J., et al. 2011, ApJS, 192, 14
Jarosik, N., Bennett, C. L., Halpern, M., et al. 2003, ApJS, 145, 413
Kangaslahti, P., et al. 2006, in Microwave Symp., ed. J. Sowers & M. Thorburn (Piscataway, NJ: IEEE), 89
Keskitalo, R., Ashdown, M. A. J., Cabella, P., et al. 2010, A&A, 522, A94
Klein, J. R., & Roodman, A. 2005, Ann. Rev. Nucl. Part. Sci., 55, 141
Komatsu, E., Smith, K. M., Dunkley, J., et al. 2011, ApJS, 192, 18
Kovac, J. M., Leitch, E. M., Pryke, C., et al. 2002, Nature, 420, 772
Kusaka, A. 2010, in Proc. XLVth Recontres de Moriond, ed. E. Augé, J. Dumarchez, & J. T. T. Vân (Ha Noi: Thẽ Gió'i Publishers), 7
Larson, D., Dunkley, J., Hinshaw, G., et al. 2011, ApJS, 192, 16
Larson, D. L., Eriksen, H. K., Wandelt, B. D., et al. 2007, ApJ, 656, 653
Leitch, E. M., Kovac, J. M., Halverson, N. W., et al. 2005, ApJ, 624, 10
Liddle, A. R., & Lyth, D. H. 2000, Cosmological Inflation and Large-Scale Structure (Cambridge: Cambridge Univ. Press)
López-Caraballo, C. H., Rubiño-Martín, J. A., Rebolo, R., & Génova-Santos, R. 2011, ApJ, 729, 25
Lueker, M., Reichardt, C. L., Schaffer, K. K., et al. 2010, ApJ, 719, 1045
Mauskopf, P. D., Ade, P. A. R., de Bernardis, P., et al. 2000, ApJ, 536, L59

Mizugutch, Y., Akagawa, M., & Yokoi, H. 1976, in Antennas and Propagation Society Int. Symp. (Piscataway, NJ: IEEE), 2
Monsalve, R. A. 2010, Proc. SPIE, 7741, 77412M
Montroy, T. E., Ade, P. A. R., Bock, J. J., et al. 2006, ApJ, 647, 813
Netterfield, C. B., Ade, P. A. R., Bock, J. J., et al. 2002, ApJ, 571, 604
Newburgh, L. 2010, Proc. Twelfth Marcel Grossmann Meeting on General Relativity, in press
Padin, S., Shepherd, M. C., Cartwright, J. K., et al. 2002, PASP, 114, 83
Page, L., Hinshaw, G., Komatsu, E., et al. 2007, ApJS, 170, 335
Pardo, J., Cernicharo, J., & Serabyn, E. 2001, IEEE Trans. Antennas Propag., 49, 1683
Sievers, J. L., Achermann, C., Bond, J. R., et al. 2007, ApJ, 660, 976
Smith, K. M., & Zaldarriaga, M. 2007, Phys. Rev. D, 76, 043001
Tauber, J. A., Mandolesi, N., Puget, J.-L., et al. 2010, A&A, 520, A1
Tegmark, M. 1997, ApJ, 480, L87
Wandelt, B. D., Hivon, E., & Górski, K. M. 2001, Phys. Rev. D, 64, 083003
Weiland, J. L., Odegard, N., Hill, R. S., et al. 2011, ApJS, 192, 19
Wright, E. L., Hinshaw, G., & Bennett, C. L. 1996, ApJ, 458, L53
Wu, J. H. P., Zuntz, J., Abroe, M. E., et al. 2007, ApJ, 665, 55